Article

Developmental Cell

Dysfunction of Hair Follicle Mesenchymal Progenitors Contributes to Age-Associated Hair Loss

Graphical Abstract

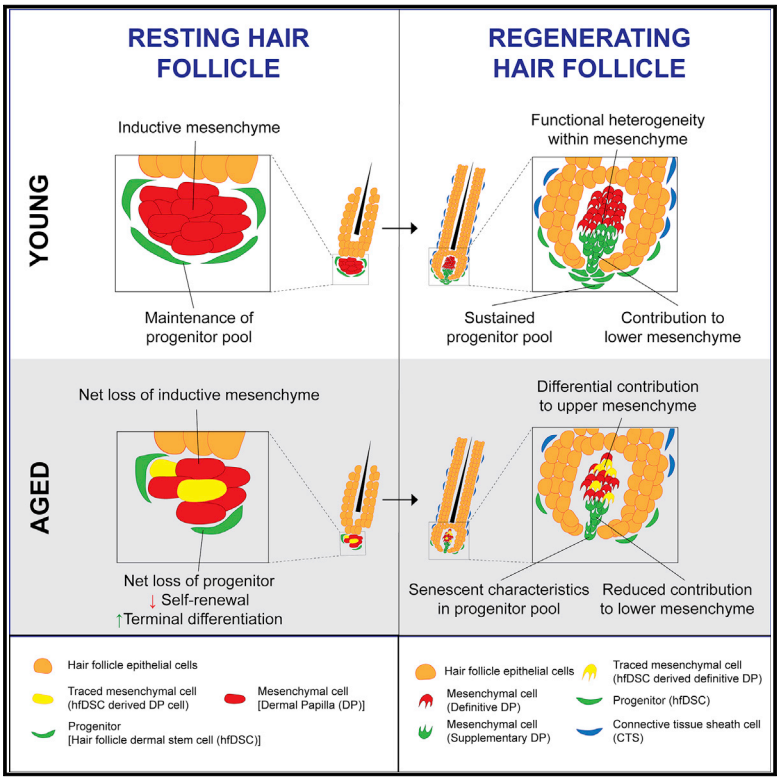

Highlights

- *In vivo* ablation of anagen DP cells initiates activation and repopulation by hfDSCs
- Single-cell RNA-seq reveals dysfunction of aged HF mesenchyme and progressive loss
- hfDSCs are seconded to replenish the DP cells in aged HFs
- Aging causes hfDSC dysfunction and depletion of the progenitor pool

Authors

Wisoo Shin, Nicole L. Rosin, Holly Sparks, ..., Elodie Labit, Jo Anne Stratton, Jeff Biernaskie

Correspondence

jeff.biernaskie@ucalgary.ca

In Brief

Shin et al. demonstrate that HF mesenchymal progenitors become dysfunctional with advanced age and are unable to repopulate the DP. This progenitor dysfunction leads to a net loss of inductive mesenchymal cells within each HF, consequently contributing to progressive hair loss.

Shin et al., 2020, Developmental Cell *53*, 185–198
April 20, 2020
https://doi.org/10.1016/j.devcel.2020.03.019

CellPress

Developmental Cell
Article

Dysfunction of Hair Follicle Mesenchymal Progenitors Contributes to Age-Associated Hair Loss

Wisoo Shin,[1] Nicole L. Rosin,[1,5] Holly Sparks,[1,5] Sarthak Sinha,[1] Waleed Rahmani,[1] Nilesh Sharma,[1] Matt Workentine,[1] Sepideh Abbasi,[1] Elodie Labit,[1] Jo Anne Stratton,[1,2] and Jeff Biernaskie[1,2,3,4,6,*]
[1]Department of Comparative Biology and Experimental Medicine, Faculty of Veterinary Medicine, University of Calgary, Calgary, AB T2N 4N1, Canada
[2]Hotchkiss Brain Institute, Cumming School of Medicine, University of Calgary, Calgary, AB T2N 4N1, Canada
[3]Department of Surgery, Cumming School of Medicine, University of Calgary, Calgary, AB T2N 4N1, Canada
[4]Alberta Children's Hospital Research Institute, University of Calgary, Calgary, AB T2N 4N1, Canada
[5]These authors contributed equally
[6]Lead Contact
*Correspondence: jeff.biernaskie@ucalgary.ca
https://doi.org/10.1016/j.devcel.2020.03.019

SUMMARY

Skin aging is accompanied by hair loss due to impairments in hair follicle (HF) epithelial progenitor cells and their mesenchymal niche. This inductive mesenchyme, called dermal papilla (DP), undergoes progressive cell loss and eventual miniaturization that contributes to HF pathogenesis. Using laser ablation and fate mapping, we show that HF dermal stem cells (hfDSCs) reconstitute the damaged DP and maintain hair growth, suggesting that hfDSC dysfunction may trigger degeneration of the inductive niche. Fate mapping over 24 months revealed progressive hfDSC depletion, and *in vivo* clonal analysis of aged hfDSCs showed impaired self-renewal and biased differentiation. Single-cell RNA-seq confirmed hfDSCs as a central precursor, giving rise to divergent mesenchymal trajectories. In aged skin, hfDSCs exhibited senescent-like characteristics, and senescence-associated secretory phenotypes were identified in the aging HF mesenchyme. These results clarify fibroblast dynamics within the HF and suggest that progressive dysfunction within the mesenchymal progenitor pool contributes to age-related hair loss.

INTRODUCTION

Tissue homeostasis and regenerative function become impaired as organisms age. A primary contributor to this phenomenon is the progressive dysfunction and attrition of tissue-resident somatic stem/progenitor cells (Jones and Rando, 2011; Oh et al., 2014; Schultz and Sinclair, 2016). Intrinsic changes, such as cellular senescence (Ocampo et al., 2016), accumulation of DNA damage (Beerman et al., 2014), and local deficiencies within the stem cell niche (Carlson et al., 2008) contribute to the diminished regenerative ability of aging somatic stem cells. Interestingly, specialized mesenchymal fibroblasts reside in many stem cell niches providing continuous reciprocal signaling that maintains the dynamic behavior of stem cells (Kabiri et al., 2014; Stzepourginski et al., 2017). Despite a growing appreciation for their diverse functions and their importance in tissue maintenance and regeneration, how mesenchymal cells are affected by aging remain largely in question.

The progressive impact of aging is particularly apparent in the skin. Aged dermis undergoes a shift in activated fibroblast proportion, resulting in reduced reprogramming efficiency and wound closure rates (Mahmoudi et al., 2019). Besides dermal thinning due to reduced extracellular matrix (ECM) density and loss of dermal fibroblasts (Demaria et al., 2015; Salzer et al., 2018), both rodents and humans exhibit progressive hair loss (Matsumura et al., 2016) and a diminished capacity to regenerate the hair follicle (HF) (Chen et al., 2014; Keyes et al., 2013).

Normal HF regeneration depends on reciprocal interactions between epithelial stem/progenitors and the specialized mesenchymal fibroblasts that comprise the dermal papilla (DP) (Greco et al., 2009; Rompolas et al., 2012). DP cells provide controlled release of signaling molecules, such as Transforming growth factor-β (TGFβ), Wingless-related integration site (WNTs, bone morphogenetic proteins (BMP), and fibroblast growth factor (FGF) to instruct the proliferation and differentiation of epithelial progenitors (Oshimori and Fuchs, 2012; Rendl et al., 2005). In mice, a minimum threshold number of DP cells is required to enable entry into anagen (Chi et al., 2013). Interestingly, in humans, age-related hair loss is associated with HFs miniaturization and a concomitant reduction in the number of DP cells (Elliott et al., 1999). Thus, sustaining sufficient cell numbers within the DP appears to be critical for maintaining HF regenerative competence.).

Resident mesenchymal progenitors within each HF, the hfDSCs, actively supply new cells to the DP and regenerate the connective tissue sheath (CTS) at the onset of each anagen growth phase (Rahmani et al., 2014). Recently, it was shown that aged interfollicular dermal fibroblasts exhibit a loss of transcriptional identity and acquire aberrant adipogenic traits (Salzer

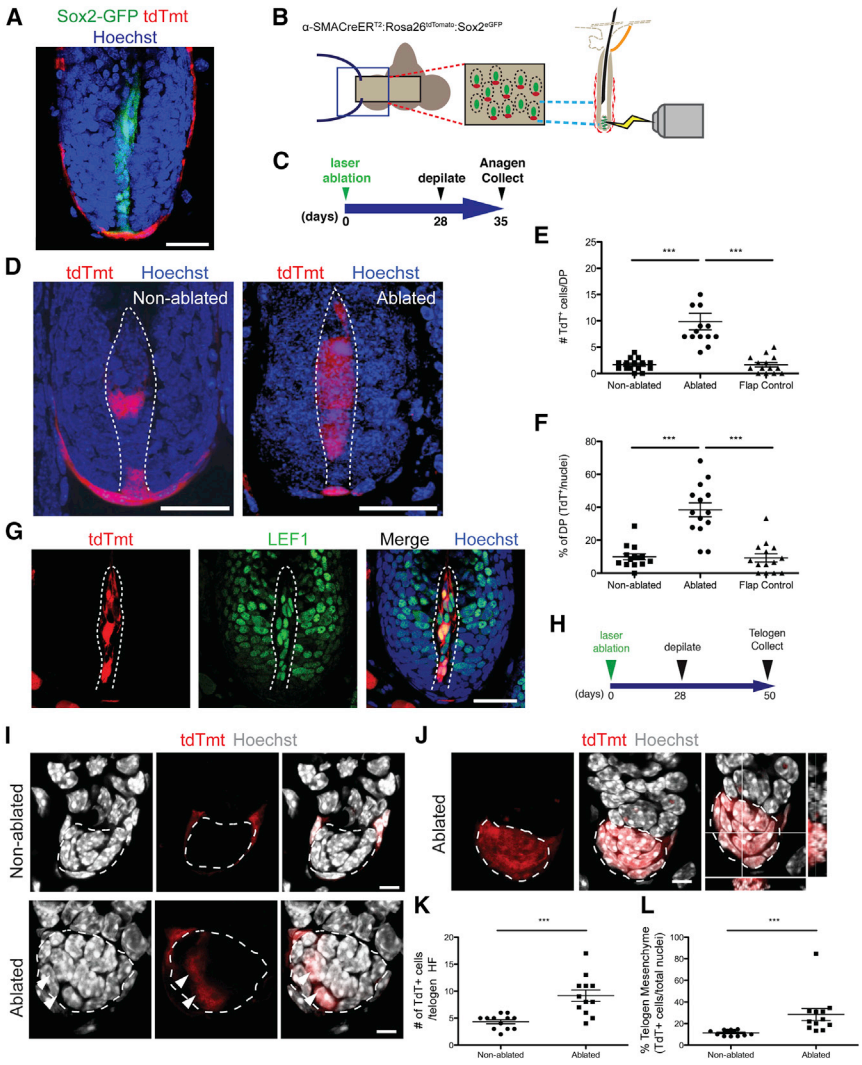

Figure 1. hfDSCs Regenerate the Damaged DP following Laser Ablation

(A) Anagen HF from an αSMA^{Tmt}:$Sox2^{GFP}$ mouse. Scale bar represents, 25 μm.

(B) Schematic describing the intravital imaging and cell ablation protocol. A detailed protocol is found in STAR Methods.

(C) Experimental timeline for anagen analysis.

(D) A non-ablated (left) and ablated anagen HF (right) from $\alpha SMA^{Tmt}Sox2^{GFP}$ mouse at 35 days post-ablation. DP is outlined by white dashed lines. Scale bar represents 25 μm.

(E) Number of TdT+ cells per anagen DP (n = 14 HFs from three mice per group).

(F) Percentage of anagen DP cells that are TdT+ (n = 14 HFs from three mice per group).

(G) TdT+ hfDSC progeny (red) populating the damaged DP co-express LEF1 (green). Scale bar represents 25 μm.

(H) Experimental timeline to analyze hfDSC behavior over consecutive hair cycles.

(I) Non-ablated (top) and ablated HFs (bottom) in 2nd telogen post-ablation. DP is outlined in dashed lines and arrows indicate TdT+ (red) DP cells. Scale bar represents 5 μm.

(J) Orthogonal image of an ablated telogen HF showing near-complete regeneration of the DP by TdT+ hfDSC progeny (red). Scale bar represents 5 μm.

(K) Number of TdT+ cells per telogen HF (n = 11 HFs from two mice per group).

(L) Percentage of TdT+ DP cells (n = 11 HFs from two mice per group). All error bars indicate ± SEM, and *p < 0.05, **p < 0.01, ***p < 0.001 derived from one-way ANOVA and Tukey's post hoc test.

et al., 2018). Based on this, we hypothesized that aging causes dysfunction of HF mesenchymal progenitors (hfDSCs), leading to diminished regenerative competence, HF degeneration, and progressive hair loss.

RESULTS

hfDSCs Regenerate the Damaged DP and Are Retained in the Definitive DP

Although hfDSCs continuously contribute new cells to the DP during each regenerative cycle (González et al., 2017; Rahmani et al., 2014), majority of cells remain in the lower region of the DP (we refer to as "supplementary DP"; Figure S1F). Thus, the extent of their regenerative capacity, their ability to reconstitute the entirety of the DP, and their ability to restore inductive function following damage remains unknown. Previously *in vivo* laser ablation of the telogen DP was reported to prevent activation of subsequent regenerative HF cycles (Rompolas et al., 2012). However, due to their close apposition with the definitive DP during telogen, it is likely that such ablation would also include hfDSCs. Thus, whether hfDSCs can be endogenously summoned to functionally replace damaged cells within the DP remains an open question.

To independently visualize DP versus hfDSC compartments, we generated α-smooth muscle actin (αSMA)CreER^{T2}:Rosa^{TdTomato}:$Sox2^{GFP}$ mice (referred to as: αSMA:Tdt:Sox2^{GFP}). $Sox2^{GFP}$ enables visualization of the DP cells, while CTS cells (including hfDSCs) can be permanently marked and fate mapped over successive HF cycles following administration of tamoxifen (4-OHT) at postnatal day 4 and 5 (Figures 1A and S1G). We then used *in vivo* laser ablation to specifically deplete the $Sox2^{GFP}$ expressing DP cells from anagen HFs, while leaving the TdT+ hfDSC population intact (Figures 1A and 1B). After ablated HFs entered telogen, we plucked the hair to initiate anagen and asked whether ablated HFs could resume normal growth in the absence of the original DP cells (Figure 1C). In a subset of HFs, the DP was largely replenished by TdT$^+$ hfDSC progeny (Figure 1D). The number of TdT$^+$ cells in anagen DP and the percentage of TdT$^+$ cells in each anagen DP were higher after laser ablation compared to HFs that did not undergo laser ablation (Figures 1E and 1F). This suggests that TdT$^+$ hfDSCs are able to replenish the damaged anagen DP. Immunostaining of hfDSC-derived TdT$^+$ DP cells confirmed the expression of the WNT-responsive transcriptional factor, LEF1 (Figure 1G), suggesting the acquisition of a true DP phenotype. This demonstrates that TdT$^+$ hfDSC

progeny, which replenish the ablated DP are functionally equivalent to definitive DP cells.

Next, we asked whether recruited hfDSC progeny persist as definitive DP cells across successive hair cycle stages or emigrate out of the DP during catagen and reintegrate into the CTS in telogen (the hfDSC niche). To answer this, we examined ablated HFs in the subsequent telogen after depilation (Figure 1H). Again, we identified TdT^+ cells within the telogen DP post-ablation (Figure 1I), and even rare HFs with DPs composed almost entirely of TdT+ hfDSC-derived DP cells (Figure 1J). There was an increase in the number of TdT+ cells per telogen HF and higher percentage of TdT+ cells comprising each telogen mesenchyme (Figures 1K and 1L). TdT+ hfDSCs that take residence within the anagen DP are retained within telogen DP over consecutive cycles and do not die nor exit to rejoin the hfDSC niche. Thus, in addition to the regenerative function of hfDSCs previously reported (Rahmani et al., 2014), hfDSCs can endogenously repair the DP after damage by acquiring a definitive, inductive DP fate. This demonstrates that the ongoing contribution of functionally competent cells by hfDSCs within the DP serve to sustain their collective inductive capacity.

Long-Term Lineage Tracing Reveals that hfDSCs Are Lost with Age

We next sought to ask whether degenerative conditions, such as natural aging, affect hfDSC number and function. We hypothesized that impaired hfDSC function contributes to the miniaturization of the DP and eventual loss of regenerative capacity observed in aging mammals (Chi et al., 2013; Elliott et al., 1999; Matsumura et al., 2016). We first confirmed the reduction in HF density by 18 and 24 months in mice (Figures S1A–S1C) and a delayed hair growth response to controlled depilation (Figures S1D and S1E), consistent with previous reports (Keyes et al., 2013; Matsumura et al., 2016). These age-associated hair phenotypes were consistently observed in all naturally aged 18- and 24-month-old B57Bl/6 mice, and in both $\alpha SMA Cre^{ERT2}$:$Rosa^{YFP}$ (referred to as αSMA:YFP) and $\alpha SMA Cre^{ERT2}$:$Rosa^{Confetti}$ (referred to as αSMA:Confetti) transgenic mice used in our report.

Tamoxifen was administered to αSMA:YFP mice at P3/4 to induce permanent expression of YFP in hfDSCs and its progeny; the HFs were analyzed at 2, 18, and 24 months for a long-term *in vivo* lineage trace analysis (Experimental Outline Figure 2A). The percentage of HFs that retained at least 1 YFP+ hfDSC during telogen steadily declined from 2 to 24 months of age, suggesting young hfDSCs are either lost or replaced with age (Figures 2B and 2C). In comparison, all arrector pili muscles, which are also marked in αSMACre:YFP mice but do not undergo cellular turnover (Fujiwara et al., 2011), always retained YFP+ cells (Figure 2C). We next assessed the total number of YFP+ hfDSCs per telogen HF between age groups. An average of 6.3 YFP+ hfDSCs encapsulated the telogen DP in 2-month-old mice, but drastically declined to 2.8 cells by 24 months (Video S1; Figures 2D and 2E). The data show a marked reduction in the number of stem cells that comprise the hfDSC pool with increasing age.

The Aging DP Is Repopulated by hfDSC Progeny

We next aimed to assess whether hfDSCs retain their capacity to repopulate the diminishing mesenchyme *in vivo*. Three-dimensional (3D) reconstruction of telogen HF mesenchyme revealed that on an average, 2-month-old telogen DPs comprised 26.6 LEF1+ cells, a known marker of telogen DP. This number declined to 16.6 cells in 24-month-old mice (Figures 2F and 2H). We also observed a striking difference in cell composition of young versus aged telogen mesenchyme. In young αSMA:YFP mice, Integrin α8+ (ITGA8+) YFP+ hfDSCs encapsulated the telogen LEF1+ DP (Video S2; Figure 2G). However, in aged αSMA:YFP mice, we consistently observed double LEF1+ YFP+ cells within the DP niche, a phenomenon occurring in only 1.0% of young HFs (Video S2; Figure 2G). The frequency of HFs containing at least 1 double LEF1+ YFP+ DP cell rose to 84.1% in 18-month-old mice and 67.7% in 24-month-old mice (Video S2; Figures 2I, S2A, and S2B). On an average, double LEF1+ YFP+ DP cells made up 17.6% and 20.0% of all DP cells in 18- and 24-month-old mice, compared with just 0.1% in 2-month-old mice (Figure 2J). We presume that these double LEF1+ YFP+ cells are terminally committed DP progeny originating from YFP+ ITGA8+ hfDSCs. Together, we show there is an overall decrease in DP cell number with age, despite ongoing contribution to the DP by terminally differentiating hfDSCs.

Aging hfDSC Progeny Persist in the Definitive DP

To determine whether the capacity of hfDSCs to acquire a definitive DP fate changes with age, we investigated the spatial distribution of YFP+ DP cells in 2-month-old versus 24-month-old anagen DPs. Auber's line, which separates the upper and lower regions of the DP, was used to define two distinct regions: upper DP (definitive DP) and lower DP (supplementary DP). In 2-month-old anagen HFs, 93.0% of YFP+ cells in the DP were found in the supplementary compartment, while only 7.0% were in the definitive DP (Figures 2K and 2L). In contrast, 56.1% of YFP+ cells were located within the definitive DP of 24-month-old HFs (Figures 2K and 2L, S2C, and S2D). There was also a marked decline in both the number of YFP+ cells recruited into supplementary DP and the total number of YFP+ cells retained in the dermal cup of aged HFs (Figure 2M). This data suggest hfDSCs progeny are preferentially recruited into the upper half of the DP in aged anagen HFs.

Aged hfDSCs Lose Self-Renewal and DP Differentiation Capacities

In order to determine whether the function of aged hfDSCs is compromised, we performed an *in vivo* clonal analysis of hfDSCs in 2- and 18-month-old αSMA:Confetti mice. Tamoxifen was administered to 2- and 18-month-old αSMA:Confetti mice following the onset of depilation-induced anagen (Experimental Outline Figure 3A) to label individual hfDSC clones (Figures 3B and 3C). Low-dose tamoxifen was used to ensure that one hfDSCs (a maximum of three) was labeled per follicle. The confetti reporter labeled the cells in one of ten colors, thus allowing clonal analysis of cells (Rahmani et al., 2014). Examples of clonal fates are shown in Figures 3D–3H.

In total, we analyzed the activity of 264 clones from 2-month-old mice (n = 4), and 219 clones from 18-month-old mice (n = 4). Quantification of proliferating and non-replicating quiescent hfDSCs revealed a 1.5-fold increase in the frequency of

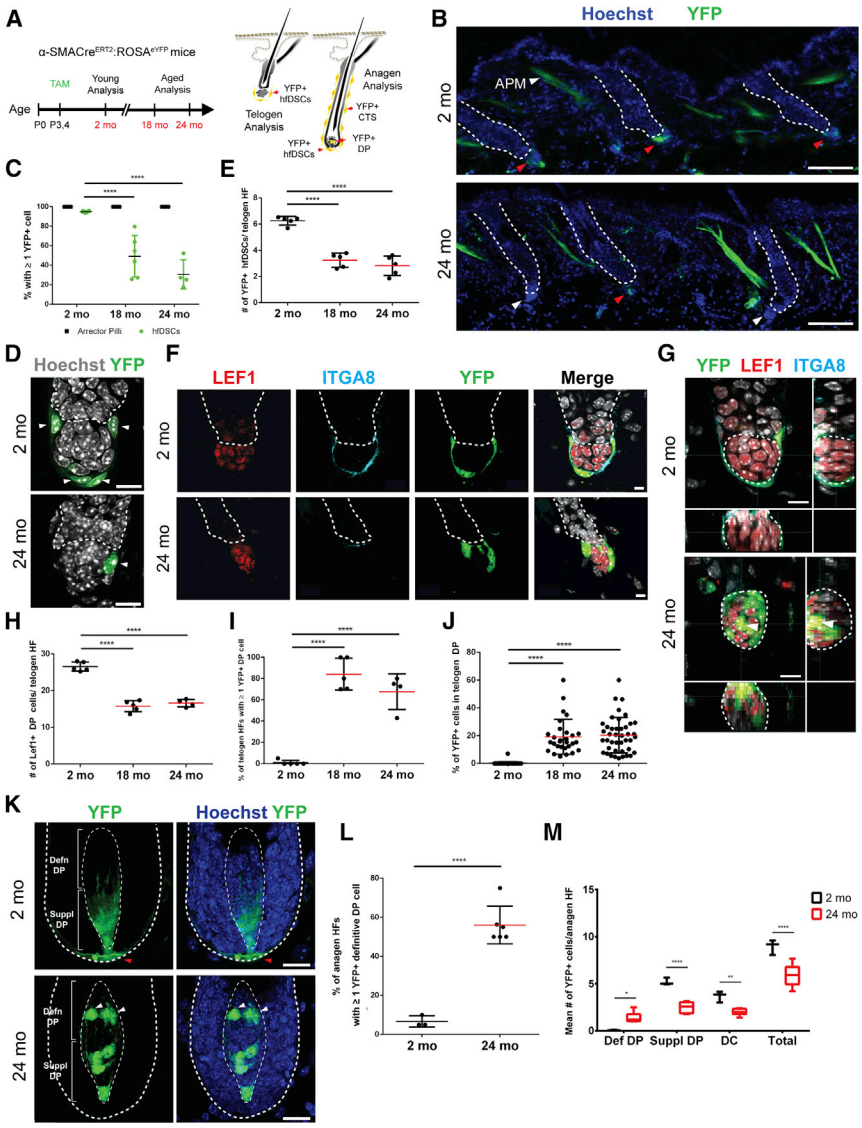

Figure 2. Long-Term Fate Mapping Reveals a Progressive Decline in hfDSC Number and Increased Recruitment to the Definitive DP with Advanced Age

(A) Schematic for the long-term lineage trace of young (2 months) versus aged (18 and 24 months) hfDSCs.

(B) Adult 2-month-old (top panel) and 18-month-old (bottom panel) αSMA:YFP mice in telogen. Red arrows indicate HFs with ≥ 1 YFP+ cell (green) in the hfDSC niche, and white arrows indicate HFs devoid of YFP+ cells. Arrector pili muscle (APM; green).

(C) Percentage of HFs and arrector pili retaining at least one YFP+ cell (n = 20 HFs/4–5 mice/groups).

(D) Telogen HF mesenchyme of αSMA:YFP mice at 2 months (top) and 24 months (bottom). Arrows indicate YFP+ hfDSCs (green).

(E) Number of YFP+ hfDSC/telogen HF (n = 20 HFs/4–5 mice/groups).

(F) Telogen HFs from 2-month-old (top) and 24-month-old (bottom) old αSMA:YFP (green) mice immunostained with LEF1 (DP; red) and ITGA8 (hfDSCs; cyan). The secondary germ is outlined in white.

(G) Orthogonal projection of telogen HFs from 2-month-old (top) and 24-month-old (bottom) αSMA:YFP mice immunostained with LEF1 (red) and ITGA8 (cyan). White arrow indicates LEF1+ and YFP+ DP cell (yellow). DP is outlined in white.

(H) Number of LEF1+ DP cells/telogen HF (n = 20 HFs/—four-five mice per groups).

(I) Percentage of telogen HFs with at least one Lef1+ YFP+ DP cell (n = 20 HFs/—four-five mice per groups).

(J) Percentage of total LEF1+ YFP+ DP cells (n = 20 HFs/—four-five mice groups).

(K) Anagen HFs from αSMA:YFP mice at 2 months (top panels) and 24 months (bottom panels) of age. Anagen DP is divided at Auber's line to define the "definitive DP" (Defn DP) and "supplementary DP" (Suppl DP). Red arrow (top) indicates hfDSCs (green) in the dermal cup (DC) and white arrow (bottom) indicates Defn DP cells above Auber's line.

(L) Percentage of HFs with at least one YFP+ DP cell above Auber's line in 2-month-old (n = 20 HFs/four animal) versus 24-month-old (n = 20HFS/six animal) mice.

(M) Number of YFP+ cells in distinct regions of the anagen HF including Def DP, Suppl DP and DC. All error bars indicate ± SD, and *p < 0.05, **p < 0.01, ***p < 0.001, one-way ANOVA and Tukey's post hoc test. Scale bars represents 100 μm (B) and 15 μm (D, F, G, and K).

quiescent hfDSCs in aged animals (Figure 3L). The most striking change was in self renewal; 49.6% of young hfDSCs underwent self-renewal compared to only 19.9% of aged hfDSCs (Figures 3I–3L). Differences in fate distribution of hfDSC progeny was also observed, as young clones gave rise to a DP cell 16.3% of the time, while only 8.0% of aged clones did so. These data corroborate with the decline in the number of hfDSC-derived supplementary DP cells in 18-month-old mice (Figure 3L). Interestingly, however, there were no significant differences in average clone size between young and aged HFs (Figure 3K). We then examined the fate of hfDSCs in telogen over two consecutive hair cycles (Figure S3A) and observed a decline in both the percentage of HFs that retained labeled cells (Figures S3B and S3C) and the percentage of expanding clones in aged mice (Figure S3D). Thus far, our long-term fate mapping and clonal analysis data demonstrate that hfDSCs undergo age-related dysfunction of both self-renewal and differentiation into DP cells.

Prospectively Isolated hfDSCs from Aged Mice Are Less Responsive to Mitogens PDGF-BB and RSPO3 *In Vitro*

To determine whether functional deficits *in vivo* are due to intrinsic changes to aged hfDSCs, we performed *in vitro* proliferation assay on prospectively isolated hfDSCs (Figure 4A). First, we identified extracellular markers ITGA8 and CD200 as extracellular markers of CTS and hfDSCs (Figure 4C). No differences were observed in fluorescence intensity or expression pattern of ITGA8 and CD200 between 2- and 18-month-old

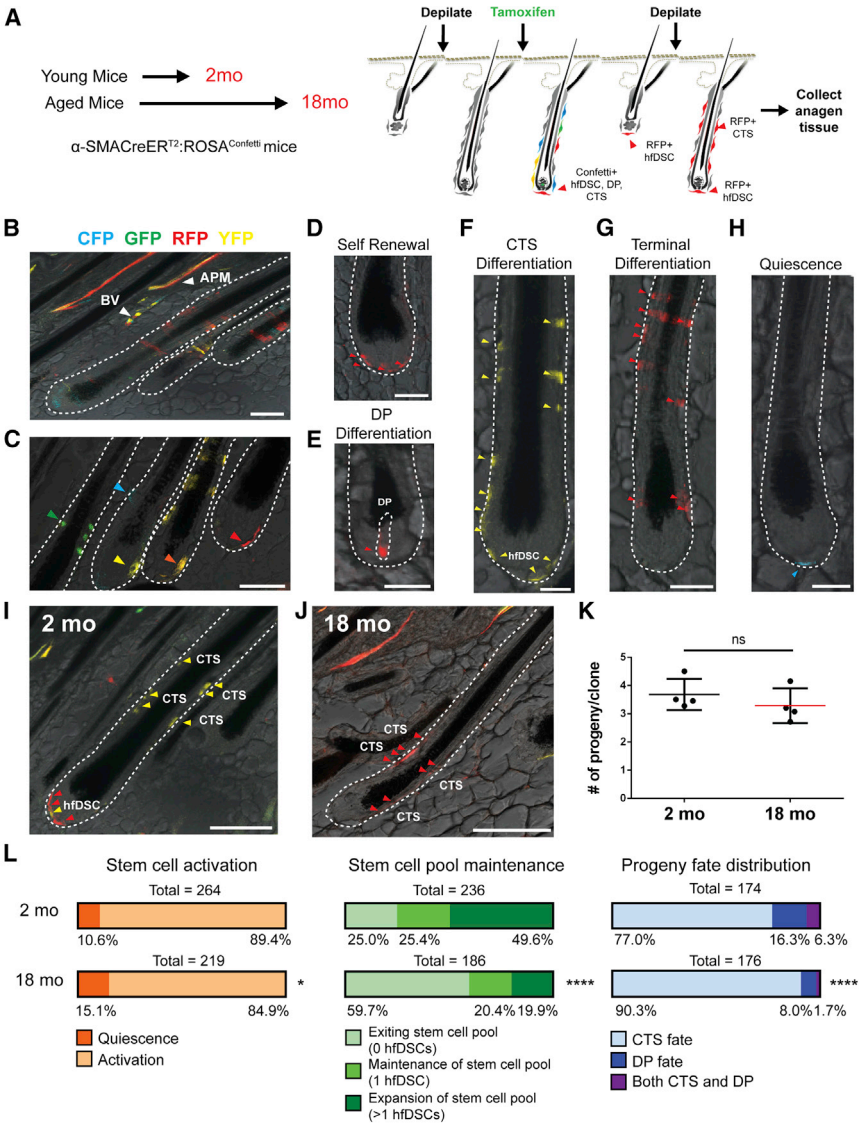

Figure 3. *In Vivo* Clonal Analysis Reveals Aged hfDSCs Exhibit Impaired Self-Renewal Capacity and Preferential Differentiation to a CTS Fate

(A) Schematic of the clonal analysis experiment using young (2-month-old) and aged (18-month-old) α*SMA*:Confetti mice.

(B) 4-OHT administration in *SMA*:Confetti mice labels mesenchymal cells within the anagen HF, arrector pili (APM) and blood vessels (BV).

(C) Representative examples of clones labeled in green (GFP), cyan (CFP), yellow (YFP), orange (YFP and RFP) and red (RFP) indicated with corresponding colored arrows.

(D) hfDSC clone exhibiting self-renewal (red); indicated by arrow.

(E) hfDSC progeny showing differentiation into DP, arrow indicates a RFP+ DP cell (red).

(F) hfDSC clone showing self-renewal and CTS differentiation, indicated by arrows (yellow).

(G) hfDSC exhibiting terminal differentiation into CTS fate, arrows indicate CTS progeny (red).

(H) hfDSC clone showing quiescence with one cell remaining at the DC, indicated by arrow (cyan).

(I and J) Anagen HFs from (I) 2-month-old and (J) 18-month-old α*SMA*:Confetti mice. Arrows indicate CTS and hfDSCs with corresponding colors.

(K) Total number of progeny generated per clone in 2-month-old (n = 264 HFs from four mice) versus 18-month-old (n = 219 HFs from four mice) HFs. Error bars are ±SD. (Two-way t test; ns= not significant.)

(L) Frequency distributions for hfDSC clonal behavior in 2- versus 18-month-old anagen HFs (n = 40–50HFs/four mice per group). Total number of HFs used in quantification are listed. "Stem cell activation," Binomial test; *p < 0.05. "Stem cell pool maintenance" and "Progeny fate distribution," chi-squared test; ****p < 0.0001. Scale bars represents 50 μm (B–H)and 100 μm (L).

mice backskin (Figures S4A–S4E). Therefore, CD200+ and ITGA8+ cells were prospectively isolated from 2- and 18-month-old mice following depilation-induced anagen using fluorescent activated cell sorting (FACS; Figures 4A and 4B). Isolated hfDSCs were grown in proliferation media (Biernaskie et al., 2009) treated with mitogens platelet-derived growth factor BB (PDGF-BB) (González et al., 2017) and Rspondin-3 (RSPO3) (Hagner et al., personal communication) to assess colony formation. There was a 3-fold decrease in spherical colony number in aged cells compared with young cells for both treatment groups in primary culture and secondary passage (Figures 4D–4G). Aged hfDSCs also generated significantly smaller colonies compared with young hfDSCs (Figures 4H and 4I), suggesting deficiencies in proliferation and self-renewal. Together, the data suggest age-related defects in hfDSCs are driven by intrinsic changes autonomous to hfDSCs, reminiscent of age-related defects in other aged somatic stem cells (Beerman et al., 2014).

Single-Cell Transcriptomics Reveal Distinct Functional Subsets within the HF Mesenchyme

To begin to understand the molecular mechanisms underlying age-associated dysfunction within hfDSCs and their progeny, we performed single-cell RNA sequencing (scRNAseq) on cells isolated from early anagen. FACS was performed to enrich for the HF mesenchyme (Figure S5A). Detailed metrics for sequencing, controls used, and analyses performed are described in STAR Methods and Figures S5 and S6. We identified 12 unique clusters (Seurat res 0.3) in our cells (Figures S5B and S5C). The top 10 markers for each population were mapped to well-established markers to identify cell types within the skin (Figures S5C and S5D; Table S1). The largest cluster (1,084 cells) was identified as DP cells, expressing *Sostdc1*, *Rspo3*, and *Fgf7* (Figures S5D and S5E) (Greco et al., 2009; Yang et al., 2017). The second largest cluster (702 cells) was CTS, identified based on *Cd200, Stmn2*, and *Ednrb* expression (Figures S5D and S5F). Importantly, the hfDSC population

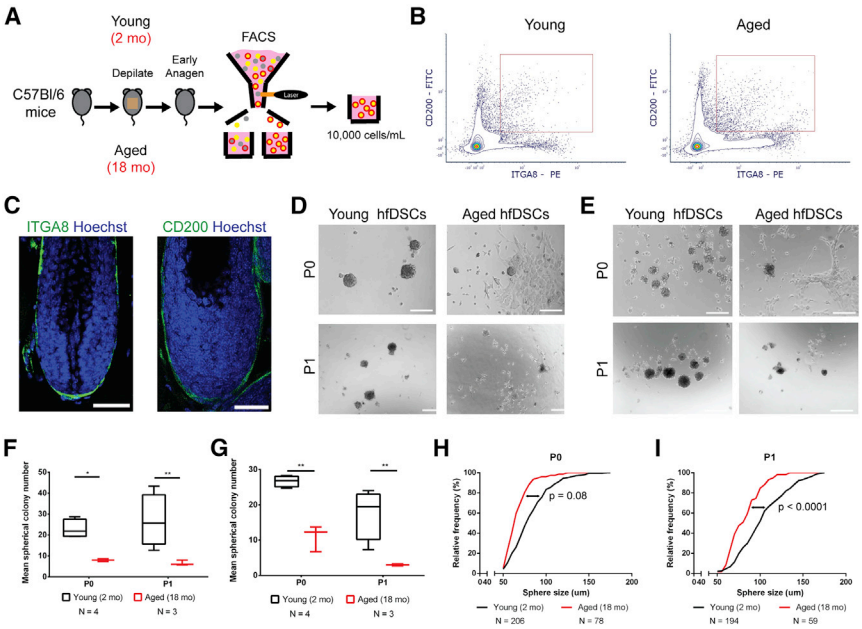

Figure 4. Prospectively Isolated hfDSCs from Aged Mice Show Diminished Proliferation in Response to Mitogens

(A) Prospective isolation of hfDSCs from 2- and 18-month-old C57Bl6 mice.

(B) FACS gating strategy to isolate $CD200^{+}$ and ITGA8+ hfDSCs from young (left) and aged (right) mice.

(C) Anagen HFs from C57BL/6 mice immunostained with ITGA8 (left panel; green) and CD200 (right panel; green).

(D and E) Young and aged hfDSCs in primary (P0) and passage 1 (P1) exposed to PDGF-BB (D) or RSPO3 (E). Scale bars represent 100 μm.

(F) Mean number of spherical colonies formed in young (n = 4) and aged (n = 3) hfDSC cultures at P0 and P1 grown in the presence of PDGF-BB (F) or Rspo3 (G).

(H and I) Cumulative frequency distribution of sphere size in (H) P0 and (I) P1 cultures of young versus aged hfDSC spherical colonies. Differences between cumulative frequency distributions was done using Kolmogorov-Smirnov test. All error bars are ±SD. Two-sided t tests, *$p < 0.05$, **$p < 0.01$.

(referred to as Progenitorcluster; PRG, 117 cells), were enriched for cell cycle genes, such as *Cdk1* and *Top2a*, and expressed both CTS and DP genes (Figures S5D and S5G). The lists of top marker genes and gene ontology (GO) terms are found in Supplemental Information (Tables S1 and S2; Figure S5D).

For an in-depth transcriptomic analysis of hfDSCs and their progeny, we selectively isolated the CTS, DP, and PRG populations from the original clusters (Figure S5B) and performed a second-level clustering analysis (Seurat res 0.6; Figures 5A and 5B). A total of seven subpopulations were identified; one PRG subpopulation, two subpopulations within the original CTS cluster (CTS1-2), and four subpopulations from the original DP cluster (DP1-4; Figures 5A and 5B). Expression of previously mentioned markers were enriched in CTS (Figure 5C) and DP (Figure 5D) subpopulations. Cells within the PRG population expressed both CTS and DP makers (Figures 5C and 5D). The top differentially expressed genes for each cluster are highlighted in Figure 5E and the list of differentially expressed genes and GO terms are found in Tables S2 and S3.

Pseudotime and RNA Velocity Corroborate the Bipotent Nature of hfDSCs and Highlight a Lineage Continuum within the HF Mesenchyme

To gain insight into cell-lineage relationships within the HF mesenchyme, we employed RNA velocity, which applies RNA splicing kinetics to predict the future state of each cell on a timescale of hours to days (La Manno et al., 2018). Applying this algorithm to our Seurat generated uniform manifold approximation and projection (UMAP) plot identified two clear trajectories of differentiation from the PRG (hfDSCs) population (Figure 5F). Starting at PRGs, two separate trajectories toward the CTS and DP fates were visualized, demonstrating the bipotent nature of hfDSCs (Figure 5F). To further determine the lineage relationships within the HF mesenchyme, we performed a pseudotime projection using Monocle2. Monocle2 is an unsupervised algorithm that clarifies temporal pattern of transcriptome dynamics (Trapnell et al., 2014). The start of the trajectory (Pseudotime = 0) was populated by PRG cells, which then split into two distinct trajectories (Figure 5G). The CTS trajectory was populated by CTS1 and CTS2 cells, whereas the DP trajectory was populated with DP1-4 cells, also confirming the bipotent nature of hfDSCs (Figures 5G and 5H). Interestingly, DP2 and DP4 were found at the start of DP differentiation, while DP1 and DP3 were found at the terminal end of the trajectory, suggesting a lineage relationship even among DP subpopulations (Figure 5H). Expression of cell-cycle genes (*Cdk1* and *Top2a*) were identified at the top of the trajectory. For the CTS trajectory, *Mgp* was highest in the CTS1 population, with expression of *Acta2* and *Tnmd* increasing in CTS2. The DP specification began with an overrepresentation of *Cyr61, Wif1*, and *Frzb*, followed by increasing expression of genes *Rspo3, Fgf10*, and *Sostdc1* at the terminal end (Figure 5I). RNA velocity and Monocle2 analyses suggest that all mesenchymal populations of the HF exist in a continuum, starting at the bipotent PRG (hfDSCs) population then differentiating into CTS and DP cells.

To confirm the accuracy of the constructed lineage trajectory *in vivo*, we employed immunofluorescence staining and *in situ* hybridization via RNA Scope. EDNRB was expressed in the upper sheath but absent in the lower sheath (Figures 5J and 5J'). Markers of multiple subpopulations within a compartment (PRG, CTS1, and CTS2), such as ACAN and ITGA8, faithfully marked the entirety of the CTS (Figures 5J and 5K). *Mgp* mRNA was enriched in the lower sheath (PRG + CTS1; Figure 5L). Interestingly, low expression of ITGA8 was observed in the supplementary DP with antigen retrieval protocol but was absent within the definitive DP (Figure 5M). RUNX3, as predicted in Seurat and Monocle2, was present evenly throughout the DP (Figure 5N). Lastly, RNAScope confirmed that *Rspo3* mRNA was restricted to the definitive DP (Figure 5O). By combining scRNAseq data with RNAScope and immunofluorescence, we

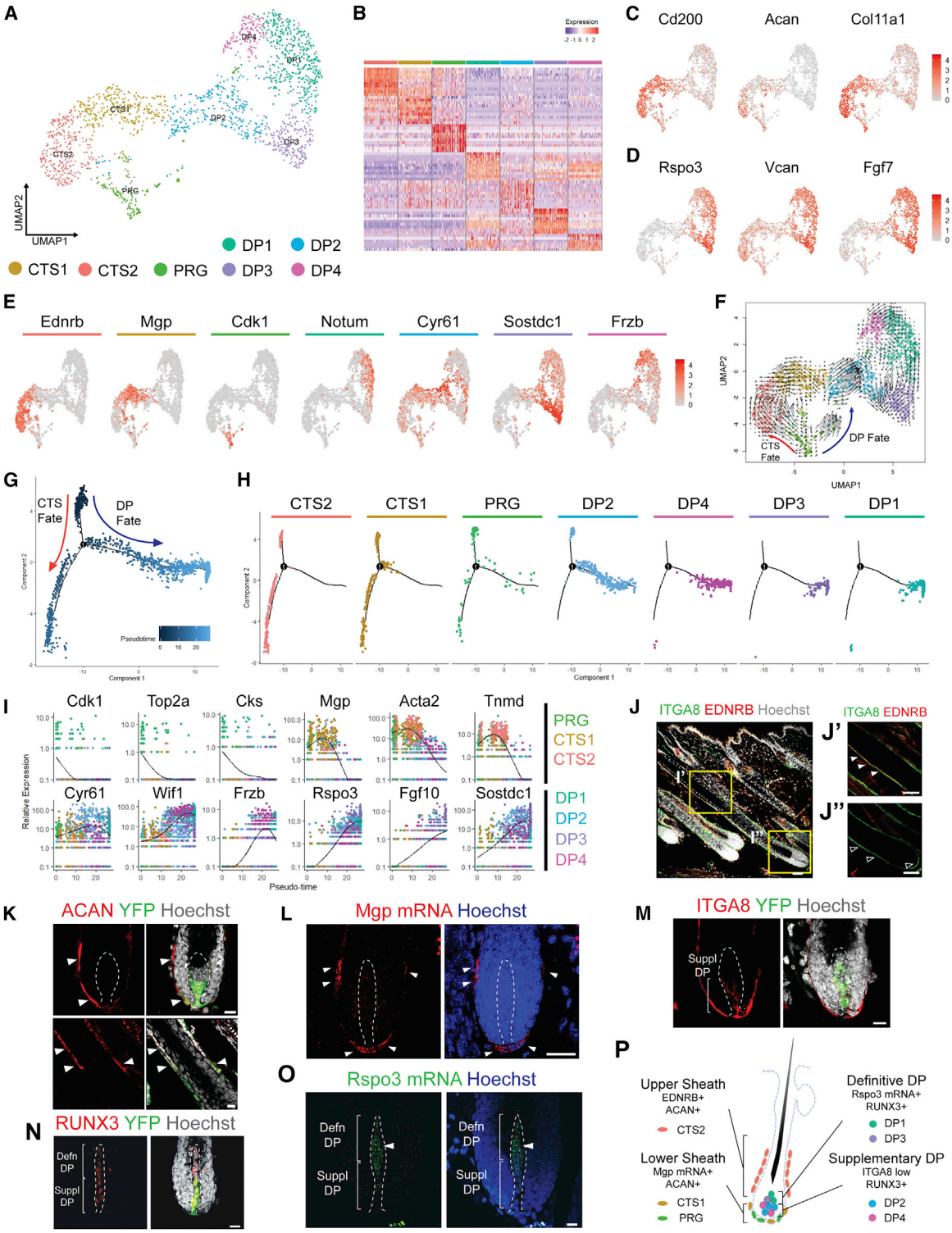

Figure 5. Single-Cell Transcriptomics and Pseudotime Analyses Reveal Distinct Functional Subsets within Each HF Mesenchymal Compartment

(A) UMAP plot of HF mesenchyme. Resolution, 0.6 in Seurat.

(B) Heatmap of the top ten differentially expressed genes ordered by adjusted p value.

(C) Expression of CTS specific markers *Cd200, Acan* and *Col11a1*.

(D) Expression of DP specific markers *Rspo3, Vcan*, and *FGF7*.

(E) The top differentially expressed genes for each of the seven subpopulations.

(legend continued on next page)

confirmed that PRG and CTS1 represent hfDSCs and CTS cells residing in the lower sheath, whereas CTS2 was indicative of the differentiated upper sheath cells (summarized in Figure 5P). DP2 and DP4 showed characteristics of the supplementary DP, while DP1 and DP3 corresponded to the definitive DP. Importantly, the four DP subpopulations identified here are congruent with the four unique DP ''microniches'' recently described by Yang et al. (2017); (Table S4). Together, our data suggest that HF mesenchymal cells exist in a continuum, confirming hfDSCs are endogenous precursors to both CTS and DP cells *in vivo* (Figures 5F–5H; summarized in Figure 5P).

Aged hfDSCs Are Less Capable of Acquiring a DP Fate and Exhibit Senescent Characteristics as Early as 12 Months of Age

Visualization of UMAP plots for young versus aged HF mesenchymal cells (Figures 6A–6C) revealed several key differences. First, there was a marked reduction in a specific proportion of dermal progenitor cells (Figures 6A and 6B; highlighted in red) that were identified as being destined to a DP fate (Figure 5F). This finding supports the loss of DP differentiation potential in aged hfDSCs *in vivo* (Figure 3L) and the reduction in contribution to supplementary DP during anagen in aged skin *in vivo* (Figure 2M). Moreover, the cell compositions of each HF mesenchymal compartment were significantly altered by advanced age. The frequency of PRG and DP4 subpopulations diminished with age, while the CTS2 population accumulated (Figures 6D and 6E). Indeed, the diminishing PRG pool, but concomitant expansion of CTS2 cells in aged HFs confirms our previous observation of hfDSC depletion and preferential acquisition of a CTS fate *in vivo* (Figures 2 and 3). Interestingly, several key genes related to WNT signaling (*Wif1, Frzb,* and *Bmp4*) as well as *Igfbp5, Ndnf*, and *Ptch1* were markedly upregulated in the DP4 population that is subsequently depleted with age (Figure 6E; Table S3). The loss of DP4 population hints that mesenchymal-epithelial signaling within aged HFs may be impaired.

CTS1 and DP1-3 showed little change in frequency (Figure 6D) but showed large differences in the gene expression between young versus aged cells (Figure 6F). Aged cells overexpressed genes involved in the AP1(JUN:FOS)-CYR61 pathway, which has been linked to fibroblast senescence and apoptosis (Figures 6F and 6G; Borkham-Kamphorst et al., 2014; Jun and Lau, 2010). Elevated expression of *Cyr61* mRNA in the aged DP and lower CTS was confirmed through *in situ* hybridization (Figure 6G). Furthermore, stress response genes *Hspa1a, Hspa1b, Hspb1, Hspa5*, and *Ubc* were highly upregulated in aged cells (>2FC; Figures 6G and 6H; Table S3). Additionally, immune cytokine (*Cxcl14*), major histocompatibility complex (*B2m*), and cell surface antigen genes (*H2-D1* and *H2-Ab1*) were upregulated, which suggests potential immune modulatory defects. Repressive genes, such as *Btg2* (anti-proliferation), *Gadd45g* (proliferation arrest), *Egr1* (tumor suppressor), and *Socs3* (suppressor of cytokine signaling) were all upregulated in aged cells. Finally, we utilized the CCInx receptor-ligand signaling analysis to evaluate changes in the signaling network within aged HFs (Figure S7I). One major change in the aging DP-epithelial matrix cell communication may be a decline in *Bmp6-Notch1* signaling, and a concomitant increase in *Fgf7-Fgfr3* signaling (Figure S7I).

To determine a potential mechanism responsible for aging in the HF mesenchyme, and in particular hfDSCs, we utilized a cell scoring algorithm in Seurat (details in STAR Methods; Tirosh et al., 2016). Established gene sets for senescence, senescence-associated secretory phenotype (SASP), autophagy, apoptosis, DNA repair, and oxidative stress response were downloaded from GSEA and KEGG databases to score the cells (Figure 6H). Surprisingly, the only differences in score between young and aged cells were in senescence and SASP (Figure 6H). Senescence-related gene expression was higher in aged PRG (hfDSCs), while aged CTS and DP cells scored highest in SASP (Figure 6I). Of aged cells, 8.79% also expressed the senescence-related transcription factor (TF), $p16^{Ink4a}$ (*Cdkn2a*), while only 3.20% of young cells expressed the gene (Figure 6J). Aged HFs stained positive for SA-β-GAL at the secondary germ and mesenchymal regions of the telogen HF (Figure 6K). These findings suggest that the mechanism driving HF mesenchyme aging may be the acquisition of senescent-like characteristics by hfDSCs.

To gain further insight into age-related transcriptional changes responsible for initiating age-related deficiencies, we FACs isolated the same mesenchymal populations from 2- and 12-month-old *αSMA*:YFP mice and performed scRNAseq (Figure S7A). Three DP, two CTS, and one PRG subpopulations were identified (Figures S7A–S7C). We found no change in the PRG population but found one accumulating and one diminishing DP subpopulation at 12 months (Figure S7D). Intriguingly, 12-month-old HF mesenchymal cells shared the transcriptional changes observed in 18-month-old cells. The accumulating DP subpopulation had substantial overexpression of *Jun, Fos, Cyr61*, and heat shock proteins (Figure S7D). The diminishing DP subpopulation was identified by *Wif1, Igfbp5*, and *Ndnf*—nearly identical to findings at 18 months (Figure S7D). Genes such as *Jun/Fos, Socs3, Klf2*, and *Klf4* were upregulated, much like the 18-months comparison (Figure S7E).

(F) RNA Velocity to predict cell state trajectories of HF mesenchymal cells. CTS fate and DP fate trajectories are highlighted.
(G) Monocle2 unsupervised pseudotime trajectory of young and aged HF mesenchymal cells. CTS and DP fate trajectories are highlighted.
(H) Pseudotime trajectory plot organized by Seurat subpopulations.
(I) Expression of CTS, DP and PRG marker genes as a function of pseudotime.
(J) Anagen HFs immunostained with ITGA8 (green) and EDNRB (red). Expression of ITGA8 and EDNRB in the (J') upper sheath and the (J'') lower sheath. Filled arrows indicate ITGA8+ EDNRB+ cells, empty arrows indicate ITGA8+ EDNRB- cells.
(K) Anagen HF from *αSMA*:YFP mice immunostained with ACAN (red).
(L) Anagen HFs stained for *Mgp* mRNA (red) via RNAScope.
(M) Anagen HF from aged *αSMA*:YFP mice immunostained with ITGA8 (red) after antigen retrieval.
(N) Anagen HF from *αSMA*:YFP mice immunostained with RUNX3 (red).
(O) Anagen HFs stained for *Rspo3* mRNA (green) via RNAScope.
(P) Summary schematic of the unique subpopulations within the HF mesenchyme. Scale bars represent 50 μm (J and L)and 15 μm (K, M, N, and O).

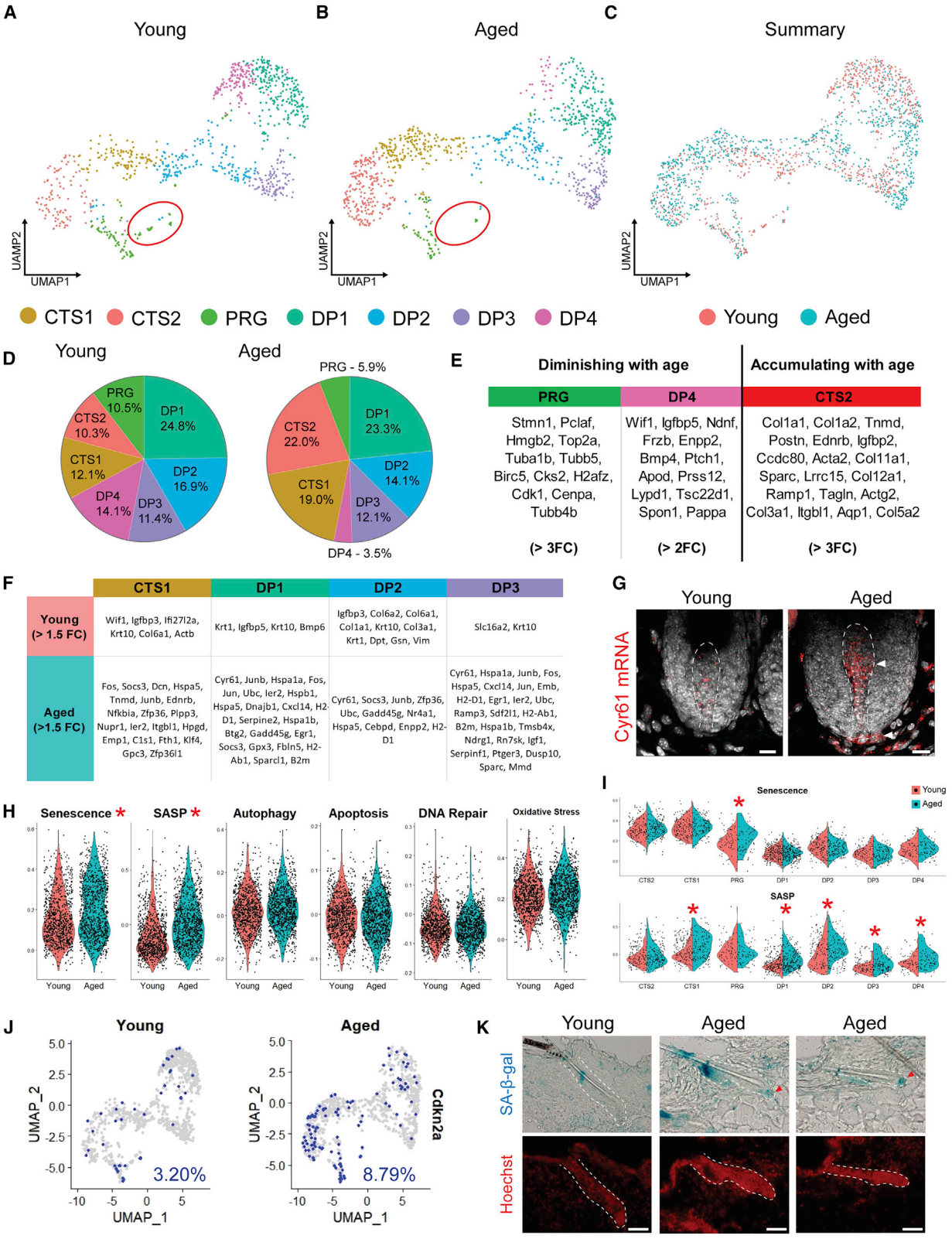

Figure 6. hfDSCs Exhibit Characteristics of Cellular Senescence and Are Depleted with Advanced Age

(A–C) UMAP plots of HF mesenchyme cells visualized by (A) young and (B) aged samples, and (C) summarized by age. The red circle indicates the absence of a DP fated PRG population.

(legend continued on next page)

12-month-old cells lost the expression of long non-coding RNA gene Maternally expressed 3 (*Meg3*; Figure S7E), which was validated through *in situ* hybridization (Figure S7F). Gene set scoring revealed that the acquisition of senescence-like characteristics by the mesenchymal progenitor pool may begin as early as 12 months of age (Figures S7G and S7H).

Aging Alters the Regulatory Network Activation within the HF Mesenchyme, Drastically Changing AP1 Transcription Factor Composition

To obtain a deeper understanding of the active gene regulatory networks (GRNs) and TF signatures that govern functional states within the HF mesenchyme, we performed single-cell regulatory network inference and clustering (SCENIC; Figure 7A). *Lef1* and *Tbx18* GRNs were restricted to DP or CTS cells, respectively, whereas *Ezh1* was active specifically in the PRG population (Figure 7B). Six unique stable states were found in our datasets (Figure 7C). *Runx3*, *Cebpa*, and *Ets1* were active in DP cells (Figure 7D). TFs active exclusively in the PRG population included *Ctcf, E2f1*, and *Tfdp1* (Figure 7D). For CTS cells, active TFs *Tead1, Hic1*, and *Tcf7l2* were identified (Figure 7D). The strength of this analysis is the ability to infer active GRN states to clusters even though simple mRNA expression may suggest a different pattern of activity (Figure 7D). Interestingly, GRNs associated with *Shh* responsive *Gli1* and embryonic *Sox18* were inferred to be active in a subset of DP cells (Figure 7E).

We identified two distinct regions overrepresented by aged cells and one region by young cells (Figure 7F). TFs involved in cell proliferation and survival (*Klf7, Egr1,* and *Egr2*), circadian rhythm (*Nfil3* and *Bhlhe40*), and telomerase regulation (*Erf*) were preferentially active in regions dominated by aged cells (Figure 7F). Interestingly, while both young and aged CTS cells showed active *Jund*, *Fos*, and *Jdp2* components of the AP1 TF complex, aged cells activated other AP1 components including *Fosb, Fosl2, Jun, Junb, Atf3*, and *Atf4* (Figure 7H), which strongly corroborates with the Seurat analysis (Figure 6). This finding proposes that the active AP1 composition is largely disturbed in the aged HF mesenchyme and could be a primary driver of aging in the HF mesenchyme.

DISCUSSION

Stem Cell Aging and Impact on Hair Loss

DP is required for induction and growth of the HF, yet, how this non-proliferative population is maintained or potentially repaired throughout life has remained elusive (Morgan, 2014). In rats, mechanical damage to DP led to the formation of a new DP, first hinting at a potential mesenchymal progenitor *in vivo* (Jahoda and Oliver, 1984). More recent fate mapping studies demonstrated the existence of a bipotent, self-renewing pool of cells in the lower CTS that contribute new cells to the DP at the onset of anagen (Rahmani et al., 2014). Here, by specifically ablating cells in the DP, but sparing hfDSCs, we showed that hfDSCs harbored the ability to replace damaged DP cells and maintain HF regenerative function. Although laser ablation of the DP during telogen was previously shown to prevent subsequent HF growth (Rompolas et al., 2012), this impairment was likely due to the inadvertent ablation of hfDSCs, which are closely apposed to the telogen DP. Importantly, this work demonstrates that hfDSCs act as a reservoir to actively supplement the DP during homeostasis and in response to cellular damage, to maintain cellular thresholds within the DP necessary to support HF growth.

Our long-term fate mapping data show that hfDSCs replenish both supplementary and definitive compartments of the DP as they are progressively depleted with advanced age. However, generation of DP cells at a time where self-renewal is diminished and fate choice appears biased to CTS, results in a net loss of hfDSCs. Consequently, the DP cannot be replenished once the hfDSC pool is exhausted and the progressive decline in DP cell number may ultimately trigger perpetual telogen and eventual degeneration of HFs (Chi et al., 2013; Matsumura et al., 2016). Our data are consistent with the idea that dysfunction of tissue-resident stem cells acts as an early catalyst to age-associated tissue degeneration (Blau et al., 2015; Oh et al., 2014). Although defects in epithelial HFSC population and the surrounding microenvironment have been a predominant focus in HF aging (Chen et al., 2014; Keyes et al., 2013; Matsumura et al., 2016), our findings suggest that hfDSCs are also significantly compromised, leading to progressive degeneration and eventual impairment of mesenchymal-epithelial interactions essential for HF regeneration (Yang et al., 2017).

Senescence-like Features in Aged HF Mesenchyme and hfDSCs

Cellular senescence of stem cells has emerged as a direct contributor to tissue aging (Childs et al., 2015; Ocampo et al., 2016). Acquisition of senescence-like characteristics in hfDSCs is driven, at least in part, by the *AP1-Cyr61* pathway. *Cyr61* promotes proliferation, survival, and angiogenesis during wound healing, but can also induce apoptosis and cellular senescence in fibroblasts (Jun and Lau, 2010), myocytes (Du et al., 2014), and liver myofibroblasts (Borkham-Kamphorst et al., 2014). Overexpression of *Cyr61* leads to senescence in aging muscle cells and fibroblasts through *p16Ink4a* activation (Du et al., 2014). Interestingly, *Cyr61* expression is mediated by the

(D) Population distribution percentage of seven subclusters in young and aged samples.
(E) Top marker genes ($p < 0.001$) in subpopulations diminishing (PRG and DP4) and accumulating in aged mice (CTS2).
(F) Top differentially expressed genes ($p < 0.001$ and Fold Change [FC] > 1.5) between young versus aged cells.
(G) Young and aged anagen HFs stained for *Cyr61* mRNA (red) via RNAScope. Arrows indicate *Cyr61*+ DC and DP cells. Scale bars represent 15 μm.
(H) Gene set enrichment scores for senescence, SASP, autophagy, apoptosis, DNA repair and oxidative stress between young versus aged HF mesenchymal cells.
(I) Gene set enrichment scores for senescence and SASP in young versus aged cells grouped by subpopulations. (H,I) Red asterisks indicate significant differences $p < 0.05$ by two-sided t test.
(J) The expression of *p16Ink4a* (*Cdkn2a*) in young versus aged mesenchyme.
(K) Young and aged telogen HFs stained for SA-β-Gal. Red arrows indicate high SA-β-Gal expression in the secondary germ and mesenchyme. Scale bars repersent 50 μm.

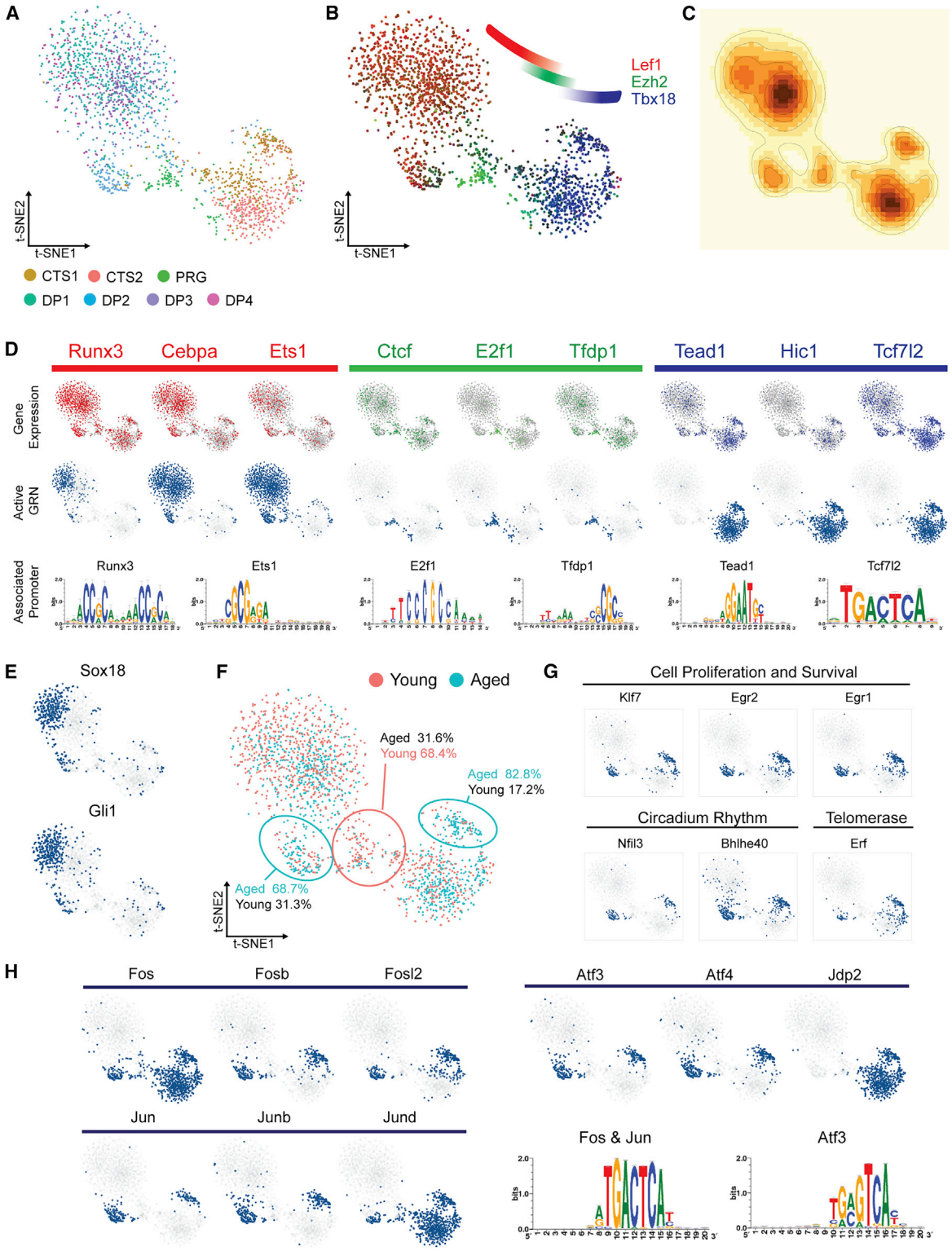

Figure 7. Gene Regulatory Network Activity Is Altered in the Aged HF Mesenchyme and Indicates Impaired Proliferative Capacity

(A) Binarized t-SNE plot of HF mesenchymal cells generated using SCENIC, colored by Seurat defined clusters.

(B) Inferred activity of *Lef1* (red), *Ezh1* (green), and *Tbx18* (blue).

(C) Density plot of stable states in the HF mesenchyme.

(D) mRNA expression for TFs specific for DP (red), hfDSCs (green) and CTS (blue), the inferred active GRN; dark blue) and the corresponding associated promoters.

(legend continued on next page)

binding of TF AP1—a heterodimer of c-Fos and c-Jun—to its cis-regulator element (Dash et al., 2010). The bulk of the aged HF mesenchyme exhibited upregulation of *Cyr61*, *Fos*, and *Jun*, and SCENIC analysis predicted that the subunit composition of the AP1 TF may be altered in aging fibroblasts. Although changes to AP1 composition and activity have been studied extensively in cancer (Hess et al., 2004), the link to aging and senescence is limited (Riabowol et al., 1992; Rose et al., 1992). Both previous studies on cultured human fibroblasts show that AP1 activity is negatively correlated with age-associated senescence, while hyperactivity of the AP1 promoter has been linked to oncogene-induced senescence (Han et al., 2018). Our data strongly suggest that aging leads to dysregulation of AP1 TF activity, driving *Cyr61* overexpression, which initiates progenitor dysfunction and eventual degeneration of the HF mesenchyme.

Enrichment of *Meg3* in the lower sheath cells of young HFs corroborates a recent report comparing gene expression in young and aged dermal fibroblasts (Salzer et al., 2018). *Meg3* is a long non-coding RNA that acts as a tumor suppressor by stabilizing and enhancing the activity of p53 (Zhu et al., 2015). Enrichment of *Meg3* in young CTS suggests that it may control hfDSC proliferation or self-renewal, and so the absence of *Meg3* in aged hfDSCs may contribute to their depletion. In contrast, *Socs3* was upregulated in aged lower CTS. *Soc3* is a downstream effector of the janus kinase and signal transducer and activator of transcription (JAK/STAT) pathway and functions to induce cytokines IL-6, IL-10, and IFN-γ. Elevated levels of *Socs3* are associated with dysfunction of aged human satellite cells, while inhibition of the JAK/STAT pathway lead to marked enhancement in satellite cell repopulation and muscle repair in aged mice (Price et al., 2014). Thus, modulating the JAK/STAT/SOCS3 pathway could potentially be targeted to stimulate the diminishing hfDSC pool in aged mice. A JAK/STAT inhibitor Ruxolitinib is able to stimulate hair regrowth in patients with alopecia areata (Mackay-Wiggan et al., 2016). Thus, Ruxolitinib may also act to mobilize hfDSCs, thereby replenishing the DP to restore inductive function.

Functional Heterogeneity in the HF Mesenchyme and the Dermal Papilla

Our transcriptomic and morphological data demonstrate functional heterogeneity across the HF mesenchyme and within the DP and CTS compartments. Recent work identified four microdomains within the DP, that serve to provide distinct instructions to neighboring epithelial and melanocyte progenitors during HF regeneration (Yang et al., 2017). Similarly, we identified four subpopulations within the DP, each with unique transcriptomic identities that show overlapping patterns in gene expression between the two datasets (Table S4). In parallel, differential recruitment of hfDSCs observed in our long-term lineage tracing suggest at least two functionally distinct compartments in the DP. Under typical regenerative conditions in young skin, hfDSCs primarily contribute progeny to the lower supplementary domain of the DP. Yet, in instances of damage, cell loss, aging, or during puberty-related HF enlargement or hair type switching (Rahmani et al., 2014), hfDSC progeny are also seconded into the upper definitive DP, which we suspect underlies the bulk of inductive function. Aging appears to preferentially impact certain subpopulations within the DP and CTS. The loss of the DP4 population results in a depletion of cells providing key signaling molecules *Wif1*, *Igfbp5*, *Ndnf*, *Frzb*, *Bmp4*, *Ptch1*, and *Spon1*. Interestingly, some of the same markers were observed to be downregulated (*Wif1*, 372-fold; *Spon1*, 164-fold) in cultured human DP cells that lost inductive capacity (Higgins et al., 2013), suggesting that aged DP cells may lose inductive capacity in similar fashion.

STAR★METHODS

Detailed methods are provided in the online version of this paper and include the following:

- KEY RESOURCES TABLE
- LEAD CONTACT AND MATERIALS AVAILABILITY
- EXPERIMENTAL MODEL AND SUBJECT DETAILS
  - Mice Handling
  - Mice Lines
  - Hair Follicle Cycle
- METHOD DETAILS
  - *In Vivo* Laser Ablation
  - Long-Term *In Vivo* Lineage Tracing
  - *In Vivo* hfDSC Clonal Analysis
  - Immunohistochemistry and Confocal Imaging
  - Orthogonal Images and Reconstructed 3D Video
  - *In Situ* Hybridization with RNAScope
  - Fluorescence Activated Cell Sorting
  - *In Vitro* Proliferation Assays
  - Cell Isolation and Single-Cell RNA-seq
  - Low Quality Cell Filtering and ScRNAseq Data Integration for 10X Chromium v2 and v3
  - Bioinformatics Analysis of Single-Cell RNA Sequencing Data Summary
  - Principle Component Calculation, Initial Clustering, UMAP Generation and Differential Gene Expression
  - Cell Cycle Scoring and Gene Set Analysis
  - Calculating RNA Velocity with Velocyto
  - Unsupervised Pseudotime Cell Ordering
  - Gene Regulatory Network analysis
- QUANTIFICATION AND STATISTICAL ANALYSIS
- DATA AND CODE AVAILABILITY
- ADDITIONAL RESOURCES

(E) The inferred active GRN (blue) of *Sox18* and *Gli1*.
(F) SCENIC t-SNE visualized by young (pink) versus aged (cyan) cells. Regions comprised predominantly young (pink) and aged (cyan) are circled, and the percentage of cells within each region are shown.
(G) Inferred active GRN (blue) of select TFs upregulated in aged cells.
(H) Inferred active GRN (blue) of AP1 TF subunits. The groups are divided in to *Fos*, *Jun*, and *Atf*/*Jdp* subunits. The most probable promoters are shown for *Fos*, *Jun*, and *Atf3*.

SUPPLEMENTAL INFORMATION

Supplemental Information can be found online at https://doi.org/10.1016/j.devcel.2020.03.019.

ACKNOWLEDGMENTS

This work was funded by grants from Canadian Institutes of Health Research (MOP-106646 and PJT-401394 to J.B.) and Calgary Firefighters Burn Treatment Society. W.S. received a Doctoral studentship from the Alberta Children's Hospital Research Institute and Alberta Innovates MD/PhD award. N.L. was a UCalgary Eyes High Postdoctoral scholar and H.S. received the Alberta Innovates Clinician-Scientist award.

AUTHOR CONTRIBUTIONS

W.S. co-wrote the manuscript, contributed to experimental design, data collection, analysis, and figure design. N.L.R. and H.S. designed, executed, and analyzed laser ablation experiments. S.S. contributed to imaging and bioinformatics analysis. W.R. contributed to experimental design. N.S. performed *in situ* hybridization protocol. M.W. assisted in bioinformatics analysis. S.A. generated transgenic mice for experiments. J.A.S. and E.L. performed single-cell processing. J.B. conceptualized experiments, co-wrote the manuscript, and supervised all experiments.

DECLARATION OF INTERESTS

The authors declare no competing interests.

Received: May 31, 2019
Revised: January 6, 2020
Accepted: March 25, 2020
Published: April 20, 2020

REFERENCES

Aibar, S., González-Blas, C.B., Moerman, T., Huynh-Thu, V.A., Imrichova, H., Hulselmans, G., Rambow, F., Marine, J.C., Geurts, P., Aerts, J., et al. (2017). SCENIC: single-cell regulatory network inference and clustering. Nat. Methods *14*, 1083–1086.

Beerman, I., Seita, J., Inlay, M.A., Weissman, I.L., and Rossi, D.J. (2014). Quiescent hematopoietic stem cells accumulate DNA damage during aging that is repaired upon entry into cell cycle. Cell Stem Cell *15*, 37–50.

Biernaskie, J., Paris, M., Morozova, O., Fagan, B.M., Marra, M., Pevny, L., and Miller, F.D. (2009). SKPs derive from hair follicle precursors and exhibit properties of adult dermal stem cells. Cell Stem Cell *5*, 610–623.

Blau, H.M., Cosgrove, B.D., and Ho, A.T.V. (2015). The central role of muscle stem cells in regenerative failure with aging. Nat. Med. *21*, 854–862.

Borkham-Kamphorst, E., Schaffrath, C., Van de Leur, E., Haas, U., Tihaa, L., Meurer, S.K., Nevzorova, Y.A., Liedtke, C., and Weiskirchen, R. (2014). The anti-fibrotic effects of CCN1/CYR61 in primary portal myofibroblasts are mediated through induction of reactive oxygen species resulting in cellular senescence, apoptosis and attenuated TGF-β signaling. Biochim. Biophys. Acta *1843*, 902–914.

Carlson, M.E., Hsu, M., and Conboy, I.M. (2008). Imbalance between pSmad3 and Notch induces CDK inhibitors in old muscle stem cells. Nature *454*, 528–532.

Chen, C.-C., Murray, P.J., Jiang, T.X., Plikus, M.V., Chang, Y.-T., Lee, O.K., Widelitz, R.B., and Chuong, C.-M. (2014). Regenerative hair waves in aging mice and extra-follicular modulators follistatin, Dkk1, and Sfrp4. J. Invest. Dermatol. *134*, 2086–2096.

Chi, W., Wu, E., and Morgan, B.A. (2013). Dermal papilla cell number specifies hair size, shape and cycling and its reduction causes follicular decline. Development *140*, 1676–1683.

Childs, B.G., Durik, M., Baker, D.J., and van Deursen, J.M. (2015). Cellular senescence in aging and age-related disease: from mechanisms to therapy. Nat. Med. *21*, 1424–1435.

Dash, R., Su, Z.Z., Lee, S.G., Azab, B., Boukerche, H., Sarkar, D., and Fisher, P.B. (2010). Inhibition of AP-1 by SARI negatively regulates transformation progression mediated by CCN1. Oncogene *29*, 4412–4423.

Demaria, M., Desprez, P.Y., Campisi, J., and Velarde, M.C. (2015). Cell autonomous and non-autonomous effects of senescent cells in the skin. J. Invest. Dermatol. *135*, 1722–1726.

Du, J., Klein, J.D., Hassounah, F., Zhang, J., Zhang, C., and Wang, X.H. (2014). Aging increases CCN1 expression leading to muscle senescence. Am. J. Physiol. Cell Physiol. *306*, C28–C36.

Elliott, K., Stephenson, T.J., and Messenger, A.G. (1999). Differences in hair follicle dermal papilla volume are due to extracellular matrix volume and cell number: implications for the control of hair follicle size and androgen responses. J. Invest. Dermatol. *113*, 873–877.

Fabregat, A., Jupe, S., Matthews, L., Sidiropoulos, K., Gillespie, M., Garapati, P., Haw, R., Jassal, B., Korninger, F., May, B., et al. (2018). The reactome pathway knowledgebase. Nucleic Acids Res. *46*, D649–D655.

Fujiwara, H., Ferreira, M., Donati, G., Marciano, D.K., Linton, J.M., Sato, Y., Hartner, A., Sekiguchi, K., Reichardt, L.F., and Watt, F.M. (2011). The basement membrane of hair follicle stem cells is a muscle cell niche. Cell *144*, 577–589.

González, R., Moffatt, G., Hagner, A., Sinha, S., Shin, W., Rahmani, W., Chojnacki, A., and Biernaskie, J. (2017). Platelet-derived growth factor signaling modulates adult hair follicle dermal stem cell maintenance and self-renewal. NPJ Regen. Med. *2*, 11.

Greco, V., Chen, T., Rendl, M., Schober, M., Pasolli, H.A., Stokes, N., Dela Cruz-Racelis, J., and Fuchs, E. (2009). A two-step mechanism for stem cell activation during hair regeneration. Cell Stem Cell *4*, 155–169.

Han, R., Li, L., Ugalde, A.P., Tal, A., Manber, Z., Barbera, E.P., Chiara, V.D., Elkon, R., and Agami, R. (2018). Functional CRISPR screen identifies AP1-associated enhancer regulating FOXF1 to modulate oncogene-induced senescence. Genome Biol. *19*, 1–13.

Hess, J., Angel, P., and Schorpp-kistner, M. (2004). AP-1 subunits: quarrel and harmony among siblings. J. Cell Sci. *117*, 5965–5973.

Higgins, C.A., Chen, J.C., Cerise, J.E., Jahoda, C.A.B., and Christiano, A.M. (2013). Microenvironmental reprogramming by three-dimensional culture enables dermal papilla cells to induce de novo human hair-follicle growth. Proc. Natl. Acad. Sci. USA *110*, 19679–19688.

Hsu, Ya-Chieh, Li, Lishi, and Fuchs, Elaine (2014). Emerging interactions between skin stem cells and their niches. Nat Med *20*, 847–856.

Jahoda, C.A.B., and Oliver, R.F. (1984). Histological studies of the effects of wounding vibrissa follicles in the hooded rat. J. Embryol. Exp. Morphol. *83*, 95–108.

Jones, D.L., and Rando, T.A. (2011). Emerging models and paradigms for stem cell ageing. Nat. Cell Biol. *13*, 506–512.

Jun, J.I.I., and Lau, L.F. (2010). The matricellular protein CCN1 induces fibroblast senescence and restricts fibrosis in cutaneous wound healing. Nat. Cell Biol. *12*, 676–685.

Kabiri, Z., Greicius, G., Madan, B., Biechele, S., Zhong, Z., Zaribafzadeh, H., Edison, Aliyev, J., Wu, Y., Bunte, R., et al. (2014). Stroma provides an intestinal stem cell niche in the absence of epithelial Wnts. Development *141*, 2206–2215.

Kanehisa, M., Furumichi, M., Tanabe, M., Sato, Y., and Morishima, K. (2017). KEGG: new perspectives on genomes, pathways, diseases and drugs. Nucleic Acids Res. *45*, D353–D361.

Keyes, B.E., Segal, J.P., Heller, E., Lien, W.H., Chang, C.Y., Guo, X., Oristian, D.S., Zheng, D., and Fuchs, E. (2013). Nfatc1 orchestrates aging in hair follicle stem cells. Proc. Natl. Acad. Sci. USA *110*, E4950–E4959.

La Manno, G., Soldatov, R., Zeisel, A., Braun, E., Hochgerner, H., Petukhov, V., Lidschreiber, K., Kastriti, M.E., Lönnerberg, P., Furlan, A., et al. (2018). RNA velocity of single cells. Nature *560*, 494–498.

Mackay-Wiggan, J., Jabbari, A., Nguyen, N., Cerise, J.E., Clark, C., Ulerio, G., Furniss, M., Vaughan, R., Christiano, A.M., and Clynes, R. (2016). Oral Ruxolitinib induces hair regrowth in patients with moderate-to-severe alopecia areata. JCI Insight *1*, e89790.

Macosko, E.Z., Basu, A., Satija, R., Nemesh, J., Shekhar, K., Goldman, M., Tirosh, I., Bialas, A.R., Kamitaki, N., Martersteck, E.M., et al. (2015). Highly parallel genome-wide expression profiling of individual cells using nanoliter droplets. Cell *161*, 1202–1214.

Mahmoudi, S., Mancini, E., Xu, L., Moore, A., Jahanbani, F., Hebestreit, K., Srinivasan, R., Li, X., Devarajan, K., Prélot, L., et al. (2019). Heterogeneity in old fibroblasts is linked to variability in reprogramming and wound healing. Nature *574*, 553–558.

Matsumura, H., Mohri, Y., Binh, N.T., Morinaga, H., Fukuda, M., Ito, M., Kurata, S., Hoeijmakers, J., and Nishimura, E.K. (2016). Hair follicle aging is driven by transepidermal elimination of stem cells via COL17A1 proteolysis. Science *351*, aad4395.

Mi, H., Muruganujan, A., and Thomas, P.D. (2013). PANTHER in 2013: modeling the evolution of gene function, and other gene attributes, in the context of phylogenetic trees. Nucleic Acids Res. *41*, D377–D386.

Morgan, B.A. (2014). The dermal papilla: an instructive niche for epithelial stem and progenitor cells in development and regeneration of the hair follicle. Cold Spring Harb. Perspect. Med. *4*, a015180.

Müller-Röver, S., Handjiski, B., van der Veen, C., Eichmüller, S., Foitzik, K., McKay, I.A., Stenn, K.S., and Paus, R. (2001). A comprehensive guide for the accurate classification of murine hair follicles in distinct hair cycle stages. J Invest Dermatol *117*, 3–15.

Nestorowa, S., Hamey, F.K., Sala, B.P., Diamanti, E., Shepherd, M., Laurenti, E., Wilson, N.K., Kent, D.G., and Berthold, G. (2016). A single-cell resolution map of mouse hematopoietic stem and progenitor cell differentiation. Blood *128*, e20–e31.

Ocampo, A., Reddy, P., Martinez-Redondo, P., Platero-Luengo, A., Hatanaka, F., Hishida, T., Li, M., Lam, D., Kurita, M., Beyret, E., et al. (2016). In vivo amelioration of age-associated hallmarks by partial reprogramming. Cell *167*, 1719–1733.e12.

Oh, J., Lee, Y.D., and Wagers, A.J. (2014). Stem cell aging: mechanisms, regulators and therapeutic opportunities. Nat. Med. *20*, 870–880.

Oshimori, N., and Fuchs, E. (2012). Paracrine TGF-β signaling counterbalances BMP-mediated repression in hair follicle stem cell activation. Cell Stem Cell *10*, 63–75.

Pineda, C.M., Park, S., Mesa, K.R., Wolfel, M., Gonzalez, D.G., Haberman, A.M., Rompolas, P., and Greco, V. (2015). Intravital imaging of hair follicle regeneration in the mouse. Nat. Protoc. *10*, 1116–1130.

Price, F.D., Von Maltzahn, J., Bentzinger, C.F., Dumont, N.A., Yin, H., Chang, N.C., Wilson, D.H., Frenette, J., and Rudnicki, M.A. (2014). Inhibition of JAK-STAT signaling stimulates adult satellite cell function. Nat. Med. *20*, 1174–1181.

Rahmani, W., Abbasi, S., Hagner, A., Raharjo, E., Kumar, R., Hotta, A., Magness, S., Metzger, D., and Biernaskie, J. (2014). Hair follicle dermal stem cells regenerate the dermal sheath, repopulate the dermal papilla, and modulate hair type. Dev. Cell *31*, 543–558.

Rendl, M., Lewis, L., and Fuchs, E. (2005). Molecular dissection of mesenchymal-epithelial interactions in the hair follicle. PLoS Biol *3*, e331.

Riabowol, K., Schiff, J., and Gilman, M.Z. (1992). Transcription factor AP-1 activity is required for initiation of DNA synthesis and is lost during cellular aging. Proc. Natl. Acad. Sci. USA *89*, 157–161.

Rompolas, P., Deschene, E.R., Zito, G., Gonzalez, D.G., Saotome, I., Haberman, A.M., and Greco, V. (2012). Live imaging of stem cell and progeny behaviour in physiological hair-follicle regeneration. Nature *487*, 496–499.

Rose, D.W., McCabe, G., Feramisco, J.R., and Adler, M. (1992). Expression of c-fos and AP-1 activity in senescent human fibroblasts is not sufficient for DNA synthesis. J. Cell Biol. *119*, 1405–1411.

Salzer, M.C., Lafzi, A., Berenguer-Llergo, A., Youssif, C., Castellanos, A., Solanas, G., Peixoto, F.O., Stephan-Otto Attolini, C., Prats, N., Aguilera, M., et al. (2018). Identity noise and adipogenic traits characterize dermal fibroblast aging. Cell *175*, 1575–1590.e22.

Schultz, M.B., and Sinclair, D.A. (2016). When stem cells grow old: phenotypes and mechanisms of stem cell aging. Development *143*, 3–14.

Stzepourginski, I., Nigro, G., Jacob, J.M., Dulauroy, S., Sansonetti, P.J., Eberl, G., and Peduto, L. (2017). CD34+ mesenchymal cells are a major component of the intestinal stem cells niche at homeostasis and after injury. Proc. Natl. Acad. Sci. USA *114*, E506–E513.

Subramanian, A., Tamayo, P., Mootha, V.K., Mukherjee, S., Ebert, B.L., Gillette, M.A., Paulovich, A., Pomeroy, S.L., Golub, T.R., Lander, E.S., and Mesirov, J.P. (2005). Gene set enrichment analysis: a knowledge-based approach for interpreting genome-wide profiles. Proc. Natl. Acad. Sci. USA *102*, 15545–15550.

Tirosh, I., Izar, B., Prakadan, S.M., Wadsworth, M.H.W., Treacy, D., Trombetta, J.J., Rotem, A., Rodman, C., Lian, C., Murphy, G., et al. (2016). Dissecting the multicellular ecosystem of metastatic melanoma by single-cell RNA-seq. Science *352*, 189–196.

Trapnell, C., Cacchiarelli, D., Grimsby, J., Pokharel, P., Li, S., Morse, M., Lennon, N.J., Livak, K.J., Mikkelsen, T.S., and Rinn, J.L. (2014). The dynamics and regulators of cell fate decisions are revealed by pseudotemporal ordering of single cells. Nat. Biotechnol. *32*, 381–386.

Yang, H., Adam, R.C., Ge, Y., Hua, Z.L., and Fuchs, E. (2017). Epithelial-mesenchymal micro-niches govern stem cell lineage choices. Cell *169*, 483–496.e13.

Zheng, G.X.Y., Terry, J.M., Belgrader, P., Ryvkin, P., Bent, Z.W., Wilson, R., Ziraldo, S.B., Wheeler, T.D., McDermott, G.P., Zhu, J., et al. (2017). Massively parallel digital transcriptional profiling of single cells. Nat. Commun. *8*, 14049.

Zhu, J., Liu, S., Ye, F., Shen, Y., Tie, Y., Zhu, J., Wei, L., Jin, Y., Fu, H., Wu, Y., and Zheng, X. (2015). Long noncoding RNA MEG3 interacts with p53 protein and regulates partial p53 target genes in hepatoma cells. PLoS One *10*, e0139790.

STAR★METHODS

KEY RESOURCES TABLE

REAGENT or RESOURCE	SOURCE	IDENTIFIER
Antibodies		
Anti-Lef1 (C12A5) antibody rabbit	Cell Signaling Technology	RRID:AB_823558
Anti-Integrin α8 antibody goat	R&D Systems	Cat# AF4076; RRID: AB_2296280
Anti-Keratin 5 antibody rabbit	Biolegend	Cat# 905504; RRID: AB_2616956
Anti-Keratin14 antibody rabbit	Biolegend	Cat# 905304; RRID: AB_2616896
Anti- Integrin α9 antibody goat	R&D Systems	Cat# AF3827; RRID: AB_2128452
Anti-Cd200 antibody rat	Abcam	Cat# Ab33734; RRID: AB_726239
Anti-Cd26 antibody rabbit	Abcam	Cat# Ab28340; RRID: AB_726291
Anti-Cyr61 antibody rabbit	Abcam	Cat# Ab24448; RRID: AB_2088724
Anti-Ednrb antibody rabbit	Abcam	Cat# Ab117529; RRID: AB_10902070
Anti-Acan antibody mouse	Invitrogen	Cat# MA3-16888; RRID: AB_568440
Anti-p16INK4a antibody rabbit	Abcam	Cat# Ab108349; RRID: AB_10858268
Conjugated Anti- Integrin α9 PE	ThermoFisher	Cat# PA5-46896; RRID: AB_2610554
Conjugated Anti-Cd200 PE	ThermoFisher	Cat# 12-5200-80; RRID: AB_1907363
Conjugated Anti- Cd26 Alexa Fluor 647	R&D Systems	Cat# FAB1180R-100UG
Goat anti-Rabbit Alexa Fluor 488/555/647	Life Technologies	NA
Goat anti-Rat Alexa Fluor 488/555/647	Life Technologies	NA
Donkey anti-Goat Alex Fluor 488/555/647	Life Technologies	NA
Anti-Runx3 antibody mouse	Dr. Yoram Groner Lab	NA
Chemicals, Peptides, and Recombinant Proteins		
Z-4-Hydroxy-tamoxifen	Sigma	H-7904
FluoSpheres	ThermoFisher	F13083
Recombinant Rspo3	R&D Systems	3500-RS
Recombinant FGF	Peprotech	100-25
Recombinant EGF	BD Biosciences	356052
Recombinant PDGF-BB	BD Biosciences	354051
Collagenase IV	Sigma-Aldrich	C5138
Dispase 5	StemCell Technologies	7913
HBSS	Gibco	14175-095
F12	ThermoFisher	11765062
DMEM	ThermoFisher	11885076
B27	Life Technologies	17504001
PenStrep	ThermoFisher	15070063
Fungizone	ThermoFisher	15290018
Fixable Viability Dye eFluor 780	eBioscience	65-0865-14
Clear Frozen Section Compound	VWR	95057-838
Permafluor Aqueous Mounting Medium	ThermoFisher	TA-006FM
Dylight 550 Fast Conjugation	Abcam	Ab201800
RNAscope Fluorescent Multiplex Reagent Kit	Advanced Cell Diagnostics	320850
Hoechst-33258	Sigma	14530
Critical Commercial Assays		
10X Genomics' Cell Ranger	10X Genomics	2.1.0, 3.0.0
BD FACS Aria III	BD BioSciences	N/A
RNAScope 2.0 HD Detection kit	ACDBio	N/A
Senescence β-Galactosidase staining kit	CellSignaling Technology	9860S

(*Continued on next page*)

Continued

REAGENT or RESOURCE	SOURCE	IDENTIFIER
Deposited Data		
Single-cell RNA sequencing raw data	Biernaskie Lab	GEO: GSE115424
Experimental Models: Organisms/Strains		
B6;129S-Sox2^{tm2Hoch}/J	Jackson Laboratories	JAX:017592
B6;Cg-Gt(ROSA)26Sor$^{tm9(CAG-tdTomato)Hze}$/J	Jackson Laboratories	JAX:007909
B6;Tg(Acta2-cre)1Rkl	Jackson Laboratories	JAX;029925
B6;*Gt(ROSA)26Sor*$^{tm1(CAG-Brainbow2.1)Cle}$/J	Jackson Laboratories	JAX:017492
B6;Gt(ROSA)26Sor$^{tm1(EYFP)Cos}$/J	Jackson Laboratories	JAX:006148
Oligonucleotides		
YFP	UofC Core DNA Services	
Cre	UofC Core DNA Services	
TdTomato	UofC Core DNA Services	
Sox2	UofC Core DNA Services	
Brainbow	UofC Core DNA Services	
Software and Algorithms		
R	R	3.6.1
RStudio	RStudio	1.1.463
CellRanger	10X Genomics	3.1.0
Seurat	Satija Lab	3.0
Monocle2	Trapnell Lab	2.4.0
SCENIC	Aerts Lab	1.0.0.3
CCInx	Bader Lab	Beta
Illustrator CC	Adobe	CC 2015
Premier Pro	Adobe	CC 2015
Photoshop CC	Adobe	CC 2015
Prism 6	GraphPad	6.01
Prism 7	GraphPad	7.01
Microsoft Excel	Microsoft	2016
FCS Express 6 Flow Research Addition	De Novo Software	6.06.0021
PANTHER 14.0	Geneontology	14.0
Imaris	Oxford Instruments	9.2.1
Other		
RNA Probe – Cyr61	ACDBio	429001
RNA Probe – Meg3	ACDBio	527201
RNA Probe – Rspo3	ACDBio	402011-C3
RNA Probe – Hspa1a	ACDBio	488351
RNA Probe - Mgp	ACDBio	463381

LEAD CONTACT AND MATERIALS AVAILABILITY

Further information and requests for resources or reagents should be directed to the corresponding author, Jeff Biernaskie (jeff.biernaskie@ucalgary.ca).

EXPERIMENTAL MODEL AND SUBJECT DETAILS

Mice Handling

All animal work was approved by the University of Calgary Health Sciences Animal Care Committee and was completed in accordance to guidelines set by the Canadian Council on Animal Care (Protocol AC-140019). Any time a 8-mm punch biopsy was taken from a mice, they were treated with 0.05mg/kg for 2 days. Both female and male mice were used in experimentation.

Mice Lines

α-SMA:YFP and α-SMA:Confetti transgenic mice have been described and published previously (Rahmani et al., 2014). The α-SMA-CreER^{T2}:Rosa^{TdTomato} mice were crossed with Sox2^{GFP+} mice to generate α-SMACreER^{T2}:Rosa^{TdTomato}: Sox2^{GFP} mice. Details of the mouse origins can be found in "Key Resources Table".

Hair Follicle Cycle

The hair cycle stage determined based on previous publications (Hsu et al., 2014; Müller-Röver et al., 2001). Hair cycles vary among ages, strains, sexes and individuals. Therefore, stages at approximately 7 days after depilation for young and 9 days after depilation for aged were used to collect comparable anagen hair follicles. The regeneration cycle was carefully monitored for each experiment by assessment of skin color and thickness.

METHOD DETAILS

In Vivo Laser Ablation

Offspring of αSMACre^{ERT2}:Rosa^{TdTomato}: Sox2^{GFP+} mice were treated with 2 doses of 4-hydroxytamoxifen in 10% EtOH and 90% vegetable oil at 0.25mg/animal at p4-5. Recombination was confirmed at p10 through fluorescence microscopy. All animals from the assigned litters that were double positive for the 2 transgene and in early anagen (p28-32) were used for the experiments and randomly assigned to the collection groups. In vivo imaging and laser ablation procedures were done at the Live Cell Imaging Facility at the Snyder Institute for Chronic Disease at the University of Calgary using an upright Olympus BX61W1 FV1000 microscope equipped with a Chameleon Ti:Sapphire femtosecond pulse multiphoton laser (Coherent) and a water immersion X20 XLUMPlan FI objective (N.A. 1.0; Olympus). Animals were anesthetized with isofluorane (4% induction, 2.5% maintenance) and subcutaneously administered 0.5 μL of buprenorphine in sterile saline (0.1 mg/kg) immediately prior to the procedure and once daily for 2 days. Mice were placed on a custom heated platform and a surgical flap was made in the skin at the base of the head which was reflected to reveal the ventral surface of the skin. The flap was fixed in place and hydrated in sterile saline for the duration of the ablation procedure. To restrict ablation to DP cells, we used a X2 digital zoom and acquired serial optical slices in 2μm steps through each HF bulb and creating serial ROIs encompassing the Sox2GFP+ DP on each slice. A 900 nm laser beam was used for imaging and ablation (IR power = 2.5W). For imaging, laser power was set to 6%. For ablation, pixel density was set to 10 pixels/μm and laser power was increased to 50%. Areas undergoing ablation were marked with fluorescent beads for identification (Figure S1H). Post-ablation imaging showed that the entirety of GFP+/ tdTomato^{Neg} DP began to emit autofluorescence across all wavelengths (but not in other compartments of the HF), indicative of successful ablation (Pineda et al., 2015; Figure S1I). The field containing ablated follicles was permanently marked at each corner by an intradermal injection of fluorescent beads to allow for subsequent visualization/evaluation.

Long-Term *In Vivo* Lineage Tracing

α-SMA:YFP pups were treated in intraperitoneal with 0.25mg of 4-hydroxytamoxifen (4-OHT) in 10% EtOH and 90% vegetable oil at postnatal day 3 and 4. α-SMA:YFP mice were housed until 2 months, 18 months or 24 months of age for analysis. 8mm telogen biopsies were taken at corresponding ages and the mice were depilated 7 (2mo) and 9 (18mo) days prior to 8mm anagen biopsy collection.

In Vivo hfDSC Clonal Analysis

Untreated 2mo and 18mo α-SMA:Confetti mice were depilated and 1mg of tamoxifen was administered via intraperitoneal injections on 7,8 days (2mo) and 9,10 days (18mo) post depilation. The mice were left for 30 days after depilation for the backskin hair follicles to regress into telogen. For analysis at anagen (Figure 3A), the mice were depilated a second time and 8mm anagen biopsies were harvested at days 7 and 9 post depilation (n = 4). If more than one cell of the same colour were located at the dermal cup (DC), it represented self-renewal of hfDSCs (Figure 3D). Differentiation to the DP (Figure 3E) and CTS (Figure 3F) could be determined based on their localization in anagen. If no labeled cells were observed at the DC but were observed in either the DP or CTS, the clone was scored to have undergone terminal differentiation (Figure 3G). Lastly, if a single labeled clone was observed in the DC, the clone was identified as a quiescent stem cell (Figure 3H). For the telogen to telogen progression analysis (Figure S3A), the first 8mm telogen skin biopsies were taken 30 days after first depilation (n=3). The same mice were depilated once more and a second set of 8mm telogen biopsies were collected at 30 days after second depilation (n = 3).

Immunohistochemistry and Confocal Imaging

Back skin biopsies were fixed with 2% paraformaldehyde in phosphate buffered saline (PBS; 0.2mM and pH 7.4) overnight, washed 3X in PBS and treated in 10%, 20% and 30% sucrose in PBS overnight. Prepared biopsies were snap frozen in Clear Frozen Section Compound (VWR International). Frozen tissue blocks were sectioned using a Leica 3050s cryostat at 45μm onto Superfrost slides (Fisher) and stored at -80°C. Frozen tissue sections were rehydrated, then blocked with 10% normal serum containing 0.5% Triton-X 100 for 1 h. Primary antibodies were incubated overnight at 4°C, washed 3x with PBS and then incubated with Alexa Fluor

secondary antibodies (Invitrogen) at 1:1,000 for 1 h. After 1x PBS wash, sections were stained with 1 ug/mL of Hoechst 33258 (Thermo Fisher Scientific) for 20 min and washed again 3x in PBS before covering with Permafluor (Thermo Fisher Scientific) and a cover slip. High resolution imaging was performed with the SP8 spectral confocal microscope (Leica). Image editing was performed using the Adobe Photoshop, Adobe Illustrator and LASX software (Leica). The list of antibodies used can be found in "Key Resources Table".

Orthogonal Images and Reconstructed 3D Video

Skin tissue were collected, fixed, prepared and immunostained as mentioned above. To generate high quality images for quantification of DP cell number (Figures 2G and 2H), z-stack images were taken every 1μm through the entire depth of the DP. The entire z-stack image was used to quantify the number of cells within the DP. To generate complete 3 reconstructed videos, high resolution confocal images were taken every 0.1μm with the SP8 spectral confocal microscope (Leica). The image was transferred to the Imaris 9.2.1 software to generate individual 3D videos. The 3D videos of young and aged (Videos S1 and S2) were combined using Adobe Premiere Pro CC 2015. For quantification of DP cells, Guard hairs were removed from quantification due to unproportionally large number of DP cells and Awl, Auchene and Zigzag hairs were used (Chi et al., 2013).

In Situ Hybridization with RNAScope

Skin tissue were collected, fixed and stored as mentioned above. RNAScope 2.0 HD Detection kit was used (ACDBio) for *in situ hybridization* according to manufacturer protocol. The tissue were thawed and rehydrated with 1x PBS for 5 min. Antigen retrieval was performed in boiling Antigen Retrieval solution (ACDBio) for 5 mins and washed in 100% EtOH for 20 seconds. Protease 3 (ACBBio) was applied to tissue sections and incubated at 40°C for 30 min before washing 2x with ddH_2O. The prepared tissue was then incubated with appropriate probes for 2 h at 40°C. After washing with Wash Buffer (ACDBio), the tissue was treated with AMP 1-4 solutions for 15-40 min at 40°C according to manufacturer recommendation. The last wash buffer was applied and DAPI solution (ACBBio) was applied for 5 min before mounting with liquid based fluorescent medium for storing and imaging.

Fluorescence Activated Cell Sorting

Telogen back skin of 2 mo and 18 mo adult mice were depilated 7 and 9 days prior to collection day. Backskin was treated with 5mg/mL dispase (StemCell Technologies) in Hank's Buffered Salt Solution (HBSS; Life Technologies) for 30-45 mins at 37°C and the epidermis was peeled off from the dermis. The remaining dermis was cut into small chunks and dissociated in 2mg/mL collagenase in Ham's F12 Nutrient mixture (Thermo Fischer Scientific) for 2 h at 37°C. Cell suspensions were diluted with cold HBSS, strained through 70μm and 40μm cell filters (Falcon) and centrifuged at 280 X g. Cell pellets were re-suspended in FACS sorting buffer (1% bovine serum album in HBSS) and then incubated with Integrin α-8 (R&D Systems) and Cd200 (Abcam) primary antibodies for 45 mins. The cells were washed with FACS sorting buffer, spun down, supernatant was removed and resuspended in 1mL of FACS sorting buffer. The cells were treated with corresponding Alexa Fluor secondary antibodies (Invitrogen) for 30 mins. eFluor 780 viability dye (eBioscience) was included in the last 5 mins to exclude dead cells and debris. The cells were washed, spun and resuspended in FACS solution. FACS isolation was performed using a FACSAria III (BD Biosciences) and analyzed using FCS Express 6 software. Single colour and appropriate isotype controls were used for compensation and gating. For in vitro proliferation assay, we enriched for dermal sheath cells by prospectively isolating ITGA8+/CD200+ cells.

In Vitro Proliferation Assays

Positive hfDSCs (Itga8+ and Cd200+) were FACS-isolated directly into 48-well plates at 10,000 cells/mL concentration. Cells were grown in standard 3:1 Dulbecco's Modified Eagle's Medium (DMEM; Thermo Fisher Scientific) to F12 (Thermo Fisher Scientific) cell culture media, with additives bFGF (50ng/mL; Peprotech), B27 supplement (4%; Life Technologies), penicillin/streptomycin (2%; StemCell Technologies) and fungizone (0.4%; Thermo Fisher Scientific). Mitogens PDGF-BB (10ng/mL; BD Bioscience) or RSPO3 (200ng/mL; R&D Systems) were also included. Cells were fed every 3 days with 10× cell culture media and grown for 9 days at 37°C in 5% CO_2 incubator. The number and size of each colony were then quantified.

Cell Isolation and Single-Cell RNA-seq

The mice were aged to either young (2mo and 12mo) aged (18mo) cohorts before isolation. To isolate cells of the hair follicle mesenchyme, we utilized Fluorescence activated cell sorting (FACS). We collected two populations of cells for all samples, to a total of 10,000 cells per age cohort (N=2 per cohort). First, we collected 5000 cells that were YFP+ and (Itga9+ or Cd200+), then we collected 5000 cells that were Cd26+ and (Itga9+ or Cd200+). The two populations were mixed to generate two replicates of young (2mo_1 and 2mo_2), one replicate of 12mo and one replicate for 18mo (N=2 per cohort). Samples were processed according to 10X Genomics ChromiumTM Single Cell 3' Reagent Guidelines v2 (2mo_1 and 18mo) or v3 (2mo_2 and 12mo) Chemistry as per the manufacturer's protocol. Single cells were sorted into 0.1% BSA–PBS and partitioned into Gel Bead-In-EMulsions (GEMs) using 10xTM GemCodeTM Technology. This process lysed cells and enabled barcoded reverse transcription of RNA, generating full-length cDNA from poly-adenylated mRNA. DynaBeads® MyOneTM Silane magnetic beads were used to remove leftover biochemical reagents, then cDNA was amplified by PCR over 10 cycles. Quality control size gating was used to select cDNA amplicon size prior

to library construction. Read 1 primer sequences were added to cDNA during GEM incubation. P5 primers, P7 primers, i7 sample index, and Read 2 primer sequences were added during library construction. Quality control and cDNA quantification was performed using Agilent High Sensitivity DNA Kit. Sequencing was performed by Genome Quebec using Illumina HiSeq4000 for 2mo_1 and 18mo samples and Illumina NovaSeqS2 for 2mo_2 and 12mo samples. Our estimated doublet rate was approximately ≈3% due to loading of 10,000 cells and we achieved ~50,0000-170,000 reads/cell). Raw reads from sequencing were processed using the 10X Genomics' Cell Ranger 2.1.0 pipeline with default and recommended parameters (Zheng et al., 2017). FASTQs generated were aligned to a custom mouse reference genome using STAR algorithm where the transgene for eYFP was appended to a pre-built GRCm38.p5 package. We recovered 2727 cells for sample 1, 1906 for sample 2, 7023 for sample 3 and 5474 for sample 4 (Figure S6A).

Low Quality Cell Filtering and ScRNAseq Data Integration for 10X Chromium v2 and v3

ScRNASeq datasets were aggregated for analysis in two ways. For the young vs. aged analysis (called "v2 only"; Figure S6C), the young (2mo_1) and aged (18mo) samples were standardized to 131,525 UMI reads per cell and a median of 2,177 genes per cell with 10X Genomics' Cell Ranger 2.1.0 (Figure S6C). Low quality cells were filtered by specifying parameters of 200 - 5500 genes detected and < 20,000 UMI count. The number of low-quality cells removed can be found in Figure S6B. Batch effect was removed from the dataset with the "*scTransform()*" function available in Seurat v3, without regressing out any variables. For integrating all the samples (called "Aggregated"; Figure S6C), the samples were standardized to 52, 270 UMI reads per cells and a median of 2,484 genes per cell with 10X Genomics' Cell Ranger 3.0 (Figure S6C). Low quality cells were filtered by specifying parameters of 500–6000 genes detected, < 30,000 UMI count and < 7.5% mitochondrial genes. Cells with high mitochondrial genes percentages were filtered out, as it can be representative of dead cells. The summary of sample details can be found in Figures S6A–S6E.

Bioinformatics Analysis of Single-Cell RNA Sequencing Data Summary

The following R-based packages were utilized for scRNAseq analysis: Seurat v3 (Macosko et al., 2015), Monocle2 (Trapnell et al., 2014), RNA Velocity (La Manno et al., 2018) and SCENIC (Aibar et al., 2017). The published online tutorials available on independent lab websites or GitHub pages for each package was followed in analyzing the dataset. For Gene Ontology analysis, PANTHER Database (Mi et al., 2013) was used with statistical overrepresentation setting. Details on the specific versions used are found in "Key Resources Table".

Principle Component Calculation, Initial Clustering, UMAP Generation and Differential Gene Expression

Before analysis, the dataset was normalized and scaled using Seurat v3. *FindVariableFeatures()* and *RunPCA()* functions were used to identify variable genes calculate the principle components. From all calculated PCs, only the top 15 PCs were used for *FindNeighbors(), FindClusters(), RunTSNE()* and *RunUMAP()* functions. Resolution of 0.6 was used for *FindClusters()*. Once clusters were generated, the *FindAllMarkers()* function with "negbinom" option to identify differentially expressed genes with p values lower than 0.01 and fold change of 2 or higher. For analyzing HF associated mesenchymal cells, clusters identified as "Connective Tissue Sheath", "Dermal Papilla" and "Progenitor" were isolated using the *subset()* function. Then new variable features and PCs were calculated, and *FindCluster()* function was run with a resolution of 0.3. *FindAllMarkers()* and *FindMarkers()* between young vs. aged samples were utilized to identify differentially expressed genes.

Cell Cycle Scoring and Gene Set Analysis

Seurat's cell cycle scoring function *CellCycleScoring()* was utilized to score all cells in one of G1, G2/M or S phases to identify dividing cells. This cell scoring strategy was derived from Tirosh et al. (2016), and the genes used in each set are derived from Nestorowa et al. (2016). Likewise, the *AddModuleScore()* function was used to score all cells based on their average expression of genes within the corresponding gene set found on Gene Set Enrichment Analysis (GSEA; Subramanian et al. (2005), Kyoto Encyclopedia of Genes and Genomes (KEGG; Kanehisa et al. (2017) or Reactome (Reactome.org; Fabregat et al. (2018). The cell scoring algorithm evaluates the expression of all genes in an input list and compares it against the expression of 100 random genes to generate a score for the state of a cell; the higher the score, the more likely the cell is undergoing a certain defined process. After retrieving from the database, each gene set was curated to remove genes that were not found in our scRNAseq dataset. The curated lists of genes are listed:

Apoptosis (KEGG, hsa04210): Aifm1, Akt1, Akt2, Akt3, Apaf1, Atm, Bad, Bax, Bcl2, Bcl2L1, Bid, Birc2, Birc3, Capn1, Capn2, Casp3, Casp6, Casp7, Casp8, Casp9, Cflar, Chp1, Chp2, Chuk, Csf2Rb, Cycs, Dffa, Dffb, Endod1, Endog, Exog, Fadd, Fas, Ikbkb, Ikbkg, Il1A, Il1B, Il1R1, Il1Rap, Il3Ra, Irak1, Irak2, Irak3, Irak4, Map3K14, Nfkb1, Nfkbia, Ngf, Pik3Ca, Pik3Cb, Pik3Cd, Pik3Cg, Pik3R1, Pik3R2, Pik3R3, Pik3R5, Ppp3Ca, Ppp3Cb, Ppp3Cc, Ppp3R1, Prkaca, Prkacb, Prkar1A, Prkar1B, Prkar2A, Prkar2B, Prkx, Rela, Ripk1, Tnf, Tnfrsf10B, Tnfrsf1A, Trp53, Tradd, Traf2, Xiap.

Autophagy (KEGG, hsa04140): Atg12, Atg3, Atg4A, Atg4B, Atg4C, Atg4D, Atg5, Atg7, Becn1, Becn2, Gabarap, Gabarapl1, Gabarapl2, Ifna1, Ifna10, Ifna13, Ifna14, Ifna16, Ifna17, Ifna2, Ifna21, Ifna4, Ifna5, Ifna6, Ifna7, Ifna8, Ifng, Ins, Pik3C3, Pik3R4, Prkaa1, Prkaa2, Ulk1, Ulk2, Ulk3.

DNA Repair (GSEA, M18229): Apex1, Apex2, Ccnh, Cdk7, Cetn2, Cul4A, Cul4B, Ddb1, Ddb2, Ercc1, Ercc2, Ercc3, Ercc4, Ercc5, Ercc6, Ercc8, Exo1, Fen1, Gtf2H1, Gtf2H2, Gtf2H3, Gtf2H4, Gtf2H5, Hmgb1, Lig1, Lig3, Mbd4, Mlh1, Mlh3, Mnat1, Mpg, Msh2,

Msh3, Msh6, Mutyh, Neil1, Neil2, Neil3, Nthl1, Parp1, Parp2, Parp3, Parp4, Pcna, Polb, Pold1, Pold2, Pold3, Pold4, Pole, Pole2, Pole3, Pole4, Poll, Rad23A, Rad23B, Rbx1, Rfc1, Rfc2, Rfc3, Rfc4, Rfc5, Rpa1, Rpa2, Rpa3, Smug1, Ssbp1, Tdg, Ung, Xpa, Xpc, Xrcc1.

Oxidative stress (GSEA, M3223): Angptl7, Aptx, Atox1, Ccl5, Cygb, Dhcr24, Dusp1, Ercc1, Ercc2, Ercc3, Ercc6, Ercc8, Gclc, Gclm, Glrx2, Gpx3, Gss, Ipcef1, Msra, Ndufa12, Ndufa6, Ndufb4, Ndufs2, Ndufs8, Nudt1, Oxsr1, Pdlim1, Pnkp, Prdx2, Prdx5, Prdx6, Prnp, Rnf7, Scara3, Sod1, Sod2, Srxn1, Stk25, Txnrd2.

Senescence (GSEA, M9143): Aldh1A3, Ctgf, Ccnd1, Cd44, Cdkn1A, Cdkn1C, Cdkn2A, Cdkn2B, Cdkn2D, Cited2, Cltb, Col1A2, Creg1, Cryab, Cxcl14, Cyp1B1, Eif2S2, Esm1, F3, Filip1L, Fn1, Gsn, Guk1, Hbs1L, Hps5, Hspa2, Htatip2, Igfbp2, Igfbp3, Igfbp4, Igfbp5, Igfbp6, Igfbp7, Igsf3, Ing1, Irf5, Irf7, Isg15, Map1Lc3B, Map2K3, Mdm2, Ndn, Nme2, Nrg1, Optn, Rab13, Rab31, Rabggta, Rac1, Rbl2, Rgl2, Rhob, Rras, S100A11, Serpinb2, Serpine1, Smpd1, Smurf2, Sod1, Sparc, Stat1, Tes, Tfap2A, Tgfb1I1, Thbs1, Tnfaip2, Tnfaip3, Trp53, Tspyl5, Vim.

Senescence Associated Secretory Phenotype (SASP; Reactome, R-HSA-2559582): Cdh1, Cdk4, Cdk6, Cdkn1A, Cdkn2A, Cdkn2B, Cdkn2C, Cebpb, Ehmt1, Ehmt2, Erk1, Erk2, Fos, Igfbp7, Il1A, Il6, Jun, Nfkb1, Nfkb2, Rps6Ka1, Rps6Ka2, Rps6Ka3, Stat3.

SASP 2 (GSEA, M27187): Anapc1, Anapc10, Anapc11, Anapc15, Anapc16, Anapc2, Anapc4, Anapc5, Anapc7, Ccna1, Ccna2, Cdc16, Cdc23, Cdc26, Cdc27, Cdk2, Cdk4, Cdk6, Cdkn1A, Cdkn1B, Cdkn2A, Cdkn2B, Cdkn2C, Cdkn2D, Cebpb, Ehmt1, Ehmt2, Fos, Fzr1, H2Afj, H2Afv, H2Afx, H2Afz, H3F3A, H3F3B, Hist1H2Ab, Hist1H2Ac, Hist1H2Ad, Hist1H2Ae, Hist1H2Bb, Hist1H2Bc, Hist1H2Be, Hist1H2Bf, Hist1H2Bg, Hist1H2Bh, Hist1H2Bj, Hist1H2Bk, Hist1H2Bm, Hist1H2Bn, Hist1H3A, Hist1H3D, Hist1H3E, Hist1H3F, Hist1H3G, Hist1H3H, Hist1H3I, Hist1H4A, Hist1H4B, Hist1H4C, Hist1H4D, Hist1H4F, Hist1H4H, Hist1H4J, Hist1H4K, Hist1H4L, Hist2H2Ac, Hist2H2Be, Hist4H4, Igfbp7, Il1A, Il6, Jun, Mapk1, Mapk3, Mapk7, Nfkb1, Rela, Rps27A, Rps6Ka1, Rps6Ka2, Rps6Ka3, Stat3, Uba52, Ubb, Ubc, Ube2C, Ube2D1, Ube2E1.

Calculating RNA Velocity with Velocyto

The standard Velocyto and velocyto.R vignettes were followed. The Velocyto software was installed as recommended and the *velocyto()* function with standard settings was used to realign the raw reads with intron and exon annotated genome from 10X Genomics. This was done for the 2mo_1 and 18mo samples separately. Once the aligned.loom files were generated, the two files were merged using the *loompy.combine*() function. The combined.loom file was then transferred into Seurat, where the data were processed and read with velocyto.R and SeuratWrappers packages. The aligned reads were then normalized, scaled and batch corrected (*SCTransform()*) and RNA Velocity was estimated using the *RunVelocity()* function.

Unsupervised Pseudotime Cell Ordering

To order cells based on gene expression in unsupervised fashion, the raw count table was exported from Seurat with ''identity'' and ''orig.ident'' in the metadata into Monocle2 with the *Negnomial()* option as the distribution algorithm. No other information was exported from Seurat. Next, low quality cells were eliminated. *dpFeature()* workflow was followed to eliminate genes that are expressed by lower than 5% of cells and calculate PCs using the remaining genes. The top PCs (10 PCs) were used to initialize the t-SNE calculation. Density peak clustering algorithm was applied to cluster the cells based on their gene expression. The top 1000 differentially expressed genes between these Monocle2 generated clusters were then used to order the cells on a pseudotime trajectory. These genes were selected as ''genes that define cell progress''. The pseudotime dimension was reduced with the DDRTree option. Lastly, the cells were ordered using the ''*orderCell()*'' function and the cells were colored based on their Seurat cluster identities. The root state was defined as the branch with the largest number of ''PRG'' cells from Seurat clustering.

Gene Regulatory Network analysis

The SCENIC, AUCell, RcisTarget and GENIE3 packages were downloaded as per supplier instructions. Murine mm9 500bp upstream 7 species and Murine mm9 20kbp upstream 7 species databases were downloaded. To start the analysis, the raw count table was exported from Seurat with ''identity'' and ''orig.ident'' in the metadata. Potential targets of each transcription factor based on co-expression was identified through the SCENIC ''co-expression network'' workflow, and the potential regulons were selected based on DNA-motif analysis with RcisTarget. Only genes with higher than 6UMI counts across all cells and are available in the RcisTarget database were used in calculation. Additionally, low quality cells were filtered out. Following supplier instruction. Spearman correlation algorithm was used to calculate correlation of regulons. GENIE3 was run to then calculate the inferred gene regulator network from the raw count table. These steps are run through the *runGENIE3()*, *runSCENIC_1_coexNetwork2modules()* and *runSCENIC_2_createRegulons()* functions. Next, the network activity of each cell was calculated with AUCell. This was run through the *runSCENIC_3_scoreCells()* function. Then stable cell states were identified and regulon activity was binarized into ''on'' or ''off'' classifications using the *runSCENIC_4_aucell_binarize()* function. 50PC and 50 perplexity settings were chosen for the final t-SNE plot.

QUANTIFICATION AND STATISTICAL ANALYSIS

All statistical analyses and graphical representations were completed by the authors using Graphpad Prism 7 and Microsoft Excel 2016. For all measurements used in this report, at least three biological and technical replicates were used. For single cell analysis,

two biological replicates were used for each sample. To determine the significance between two groups, comparisons were made using unpaired 2-tailed t tests with Welch's correction. For comparison between multiple groups, one-way ANOVA multiple comparisons and Tukey post hoc tests were employed. For all tests significance was defined as p value < 0.05.

DATA AND CODE AVAILABILITY

The accession number for the scRNAseq data reported in this paper is GEO: GSE115424.

ADDITIONAL RESOURCES

None.